Master Thesis

to obtain the degree Master of Science at the

University of Graz and Technical University of Graz

Observing Atmospheric Rivers with Radio Occultation Data

Lucas Oppeneiger

2019

Supervisor: Assoz.-Prof. Mag. Dr. rer. nat. Ulrich Foelsche

Co-Supervisor: Mag. Dr. rer. nat. Julia Danzer

Wegener Center for Climate and Global Change (WEGC) and Institut for Geophysics, Astrophysics, and Meteorology/Inst. of Physics (IGAM/IP) University of Graz

Abstract

UNIVERSITY OF GRAZ

Wegener Center and Institute of Physics

Observing Atmospheric Rivers with Radio Occultation Data

Lucas Stephan Oppeneiger

Atmospheric rivers are a natural phenomenon and relatively narrow corridors of concentrated moisture in the atmosphere. Atmospheric rivers transport horizontally most of the water vapor beyond the tropics. Because of the huge amount of water vapor, extreme precipitation events as well as floodings in the mid-latitudes, including Europe and the United States, occur.

To study atmospheric rivers, data with a high vertical and horizontal resolution, as well as, global coverage are required. In this study, data gained with the Radio Occultation method and processed with the WEGC occultation processing system, version 5.6, are used. Further on, the vertical distribution of atmospheric rivers are studied.

In this thesis, four different atmospheric river events, with regard to the temporal evolution and vertical distribution are examined.

Zusammenfassung

UNIVERSITÄT GRAZ

Wegener Center und Institut für Physik

Untersuchung atmosphärischer Flüsse mit Hilfe der Radio - Okkultationsmethode

Lucas Stephan Oppeneiger

Atmospheric rivers sind Naturphänome, welche im Speziellen relativ enge Bändern, bestehend aus konzentrierter Feuchtigkeit in der Atmosphäre sind. Atmospheric rivers sind für den horizontalen Transport von Wasserdampf außerhalb der Tropen verantwortlich. Aufgrund der großen Wasserdampfmenge in der Atmosphäre treten extreme Niederschlagsereignisse sowie Überschwemmungen in den mittleren Breiten, einschließlich Europa und den Vereinigten Staaten, auf.

Um atmosphärische Flüsse zu untersuchen, sind Daten mit einer hohen vertikalen und horizontalen Auflösung, sowie eine globale Abdeckung erforderlich. In dieser Arbeit werden Daten verwendet, die mit der Radio-Okkultationsmethode gewonnen und mit dem WEGC-Okkultationsverarbeitungssystem, Version 5.6, verarbeitet wurden. Weiterhin wird die vertikale Verteilung der atmosphärischen Flüsse untersucht.

In dieser Arbeit werden vier verschiedene Ereignisse, welche von atmosphärischen Flüssen geprägt sind, hinsichtlich der zeitlichen Entwicklung und der vertikalen Verteilung untersucht.

Acknowledgement

I would like to take this opportunity to express my gratitude to all those who have accompanied me during my studies and the creation of this thesis.

First of all I want to thank my supervisor Ulrich Foelsche for giving me the opportunity to write this thesis at the Wegener Center for Climate and Global Change and the excellent mentoring through this thesis.

Furthermore, I would like to thank my co - supervisor Julia Danzer, for the support and the helpful advices in difficult situations and the help in proofreading this thesis.

I would like to express my thank to my family, especially my parents, my brother and my grandparents, who were always helpful in numerous ways.

A special thank you goes to my friends, for providing me advice and support in though situations and for the amazing moments we went through.

And finally to Martina, who has been by my side throughout my study time and this thesis and without whom, I would not have had the courage to finish this journey.

Contents

1 Introduction

The climate of the earth has always changed and the natural variability of the climate plays an essential role. But it should be noted that the climate has changed significantly and, above all, faster since the Industrial Revolution. This effect is referred to as the anthropogenic green house effect and is described in dozens of theses.
An important contribution to this is provided by the so-called Intergovernmental Panel on Climate Change [Stocker et al., 2013]. This 2013 report explains that the human impact on the climate is clear and that anthropogenic greenhouse gases have peaked. A linear trend reveals a surface temperature increase of 0.85 K $\pm$ 0.2 K from 1982 to 2012. This trend suggests that the surface of the earth will continue to warm in the 21st century. This climate change is always adding new risks to human habits and can lead to worse disasters. Connected with increasing temperature, the potential of water vapor in the atmosphere increases and severe catastrophes can be the result.
In order to understand Atmospheric rivers, it has become increasingly important to obtain more accurate atmopspheric data, which provide global coverage. The method to obtain data which are used in this thesis is based on the property of radio occultation (RO). This measurement method has the properties that are required for a good data evaluation, which would be, for example, long-term stability, all weather stability and a high vertical resolution.
As our climate changes and the risk of natural disasters increases, it is all the more important to be in possession of this data. For this reason, RO data are also used for the study of atmospheric river. But what exactly are atmospheric rivers?

Atmospheric rivers (AR) are very long, narrow bands with a very high concentration of water vapor in the atmosphere. These bands move extreme masses of water vapor to coastal areas, which can cause heavy rainfall and flooding. The water vapor is transported from the tropics in 400 to 600 kilometers narrow rivers to higher latitudes. These atmospheric rivers can stretch up to more than 2000 kilometres and can even be seen on satellite imagery (See Fig.: 1).
These atmospheric rivers can occur anywhere on Earth, but some regions are more affected than other regions of the world. Strongly affected regions are the west coast of the US, especially California and Washington, as well as the western coasts of Europe, such as Spain, the United Kingdom and Norway.
These extreme weather events can cause severe flooding, heavy snowfall and storms that cause millions of dollars worth of damage. The researcher David Lavers from the Univer-

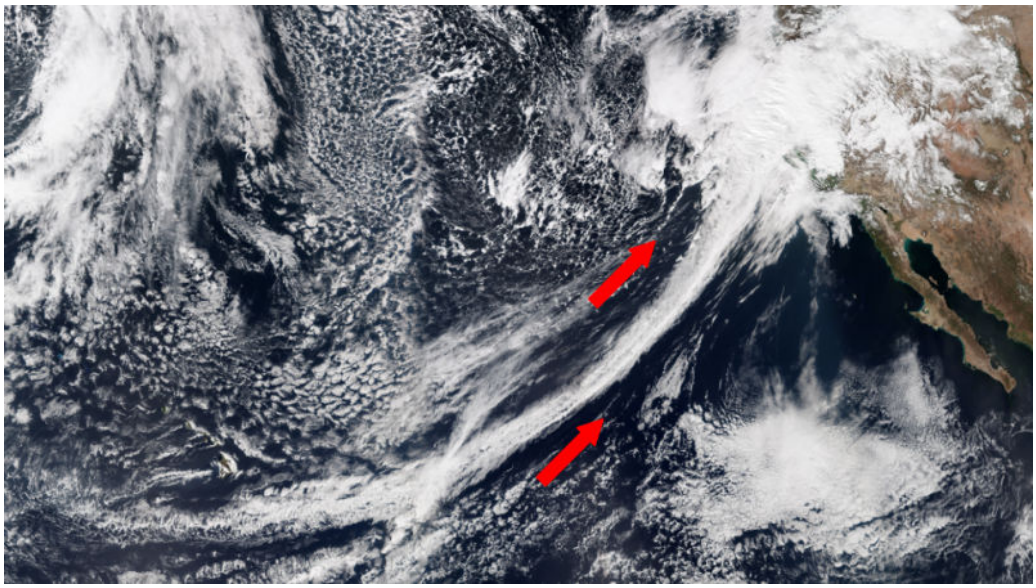

Figure 1: A satellite picture showing an atmospheric river hitting the west coast of the USA on February 22nd, 2017. Source: [Dvorsky, 2017]

sity of Reading found that the most severe floods on the British Isles since 1970 were all influenced by atmospheric rivers [Lavers et al., 2011a].

Some atmospheric rivers are so important to some regions that names have been given to the water vapor bands. One of these atmospheric rivers is the so-called „pineapple express“. This natural phenomenon hits regularly the west coast of the US, causing severe damage in this region. A closer look at this type of AR is given in chapter 3.3.

The aim of this thesis is to investigate four different cases of atmospheric river events with the RO method. The RO method is based on radio signals which penetrate the Earth's atmosphere. The phase change of the radio signal is measured at a Low Earth Orbit (LEO) satellite and further processed to thermodynamic variables such as temperature, pressure and density at different processing centers (e.g. Wegener Center at the University of Graz (WEGC)). From these variables the precipitable water (PW) can be calculated and thus atmospheric rivers can be studied.

Furthermore, the vertical distribution of AR's are analyzed to show, how high the water vapor extends into the atmosphere. This gives a closer look on the difference between the ARs and the uniqueness of each event.

Chapter 2 discusses the properties of water vapor and introduces the important physical sizes, such as specific humidity, integrated water vapor (IWV) or precipitable water. Chapter 3 contains the atmospheric rivers. It explains what the definition of atmospheric

rivers is and where they can occur. Chapter 4 introduces the radio occultation method and the retrieval of the variables is discussed. Chapter 5 takes a closer look at the used data sets for the calculations. Chapter 6 shows the results for the four selected events. Finally, a summary and an outlook on atmospheric rivers are given in Chapter 7.

2 Water vapor

Water vapor is one of the most important and most abundant gases in our atmosphere. Furthermore, it is the only molecule that can change the aggregate state in the atmosphere and thus occurs in 3 phases, namely gaseous, liquid and solid. Although water exists in the atmosphere as vapor, liquid, and solid, the vapor phase dominates. Further on, it is a greenhouse gas, that has a tremendous impact on climate change and is therefore of great importance to us humans. Each greenhouse gas, like water vapor, has its own global warming potential. The available water vapor in the atmosphere accounts up to 60% - 70% of the greenhouse effect.

2.1 Properties of water vapor

Water vapor can be generated by evaporation or boiling of liquid water or by sublimation of ice. Unlike other forms of water, water vapor is invisible. Under typical atmospheric conditions, water vapor is continuously generated by evaporation and removed by condensation. It is lighter than air and triggers convection currents that can lead to clouds. [Steiner et al., 2011]

Water vapor is the atmospheric constituent with the greatest effect on the dynamics, thermodynamics, and radiation balance of the atmosphere, it is the most abundant of the greenhouse gases in the atmosphere and the most important in establishing the Earth's climate.

The measurement of the amount of water vapor in a medium can be performed directly or remotely with varying accuracy. Remote methods such as electromagnetic absorption are possible from satellites to planetary atmospheres. Direct methods can use electronic transducers, humidified thermometers, or hygroscopic materials that measure changes in physical properties or dimensions.

2.1.1 Partial pressure of water vapor

The water vapor pressure e is the pressure that occurs when, in a closed system, a vapor with the associated liquid phase is in thermodynamic equilibrium. The water vapor pressure is the partial pressure of water vapor in the mixture of a gas and increases with rising temperature.

The partial pressure, is the pressure of each constituent in a mixture of gases. It is measured in hPa or mbar and can be described, as the sum of the partial pressures of each component. The following equation is called „Dalton's Law“and describes the overall

pressure as the sum of each partial pressure in the system.

$$p = p_1 + p_2 + p_3 + ... \tag{2.1}$$

where p is the total pressure of a mixture of non-reactive gases and p_n are the partial pressures of each component.

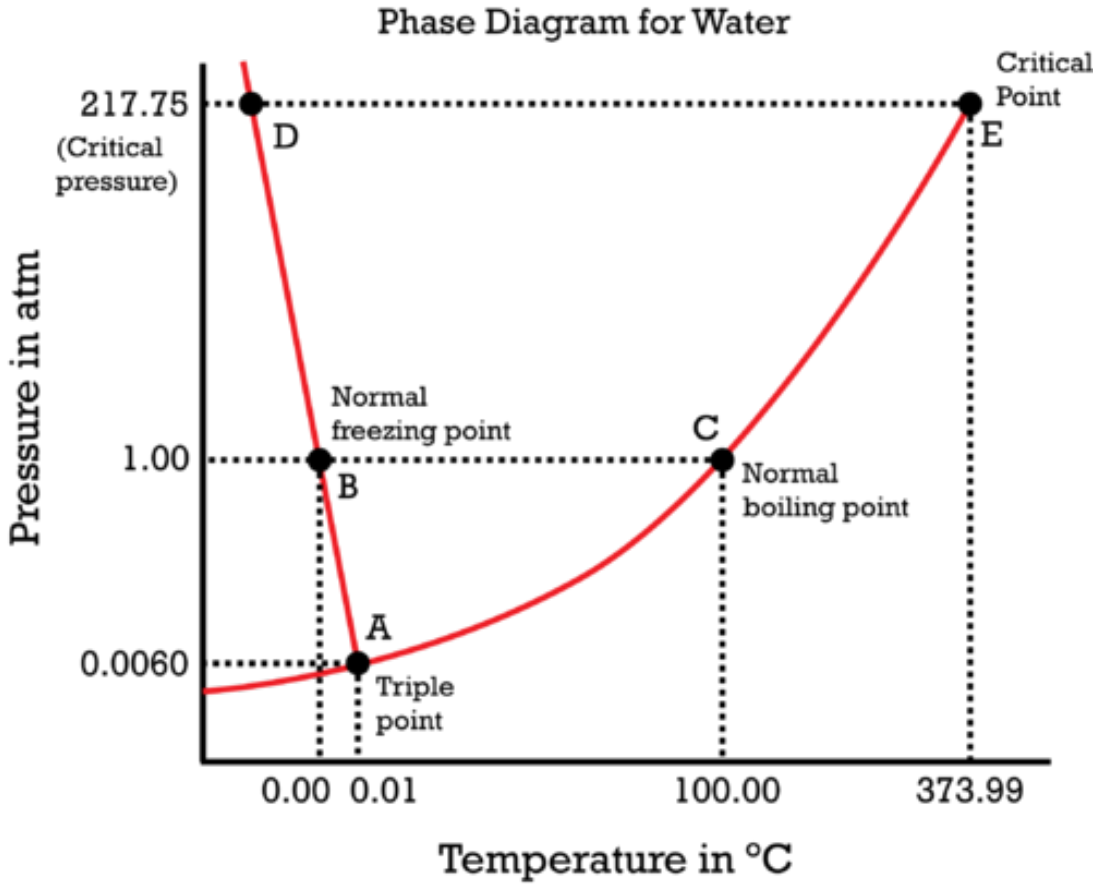

Figure 2: The phase diagram for water. The three different phases, solid, fluid and gas form, are plotted over temperature and pressure. (Taken from Auyeung, 2019)

Water can occur in three different stages: solid, liquid and gaseous. In figure 2 the phase diagram of water is demonstrated. At the figure the pressure is a function of temperature and the three different stages of water are shown. The three different lines are the vapor pressure curve, the melting curve, and the sublimation curve. They indicate the phase transition between the gaseous, liquid and solid phases. They meet in one point, called: Triple Point, which means that, all three phases of water can occur. The phase diagram is well suited to gain an overview of the phases in equilibrium under certain conditions.

2.1.2 Absolute humidity

The absolute humidity ρ_{w} is the mass of water vapor in a given volume of air. It is usually expressed in grams of water per cubic meter of air $\frac{g}{m^3}$. The absolute humidity is bounded at the top by the maximum humidity $\rho_{\mathrm{w,\,max}}$ that prevails during saturation. The water vapor pressure and absolute humidity are linked via the ideal gas law (equation of state):

$$e = \rho_{\mathrm{w}} R_{\mathrm{w}} T, \tag{2.2}$$

where $R_{\mathrm{w}} = \frac{R^*}{m_{\mathrm{w}}}$, with R^* being the universal gas constant (8.314510 ± 0.000070 Pa m^3 K^{-1} mol^{-1} or 8314.510 ± 0.070 J $\mathrm{kmol}^{-1}\mathrm{K}^{-1}$), T the absolute temperature in K, and m_{w} the molar mass of water vapor (18.01528 kg/kmol). [Foelsche, 2017]

2.1.3 Specific humidity

The specific humidity q indicates the mass of water that is in a certain mass of humid air. Hence, the specific humidity is the ratio of the mass of water vapor in a moist air parcel relative to the total mass of the moist air, expressed in kg/kg or g/kg. The numerical value range is $0 < s < 1$, where s = 0 for dry air and s = 1 for air-free steam or liquid water. If the volume of the air package increases, then both the (unchanged) mass of the moist air and the (unchanged) mass of the water vapor are distributed to a larger volume, but the ratio of the two masses in the air package remains the same.:

$$q = \frac{\rho_{\mathrm{w}}}{\rho} = \frac{m_{\mathrm{w}}}{m_{\mathrm{d}}} \frac{e}{p - (1 - \frac{m_{\mathrm{w}}}{m_{\mathrm{d}}})e}, \tag{2.3}$$

where ρ is the density of moist air, m_{d} is the molar mass of dry air (28.9644 ± 0.0014 kg/kmol), $m_{\mathrm{w}}/m_{\mathrm{d}} = 0.62198$, e is the partial pressure of the water vapor and p is the total pressure of moist air. [Foelsche, 2017]

2.1.4 Mixing ratio

The mixing ratio (m) is the amount of water vapor that is in the air divided by the mass of the dry air. It can be written as follows:

$$m = \frac{\rho_{\mathrm{w}}}{\rho_{\mathrm{d}}}, \tag{2.4}$$

2.1.5 Integrated water vapor

The integrated water vapor (IWV) is the integral over a unit area, with the upper boarder of infinity. This represents the total water in the atmosphere and is measured in mm.

$$IWV = \int_0^\infty \rho_{\mathrm{w}}(z)\mathrm{d}z, \tag{2.5}$$

2.1.6 Precipitable Water (PW)

The precipitable water is the integrated water vapor expressed as the height of the water column, if all the water in that column was precipitated as rain. It is usually measured in mm.

$$PW = \frac{IWV}{\rho_{\mathrm{l}}}, \tag{2.6}$$

where $\rho_{\mathrm{l}} = 998$ kg/m^3 is the density of liquid water at 20 °C. [Foelsche, 2017]
This equation is used to analyse atmospheric rivers in this thesis.

2.2 Water vapor in the atmosphere

Water vapor is one of the most important constituents of the atmosphere and passes through evaporation into the atmosphere, where it transforms into clouds and precipitation. The water vapor content in the atmosphere varies according to latitude and longitude and can account for about 4% of the total troposphere in the tropics. This water vapor also has an extreme impact on our climate because it is one of the strongest greenhouse gases. Without greenhouse gases, or rather the natural greenhouse effect, our planet would be hardly habitable. Without this effect, the average temperature would be instead of the pleasant 15° C at -18° C [Ma, 1998].
Water vapor plays a very important role here, because if an increase in water vapor in the atmosphere is measured, there is also a positive feedback of the greenhouse effect. The positive feedback can be explained as follows: The higher the temperature, the more water vapor can be stored in the atmosphere and the higher is the greenhouse effect.
The water vapor content in the atmosphere increased since 1988 per decade by about 0.41 kg/m^2. This can not be explained with the natural variability in the Earth's climate system. A plausible explanation for this effect is the human influence on the Earth's atmosphere. [Staff, 2007]

2.2.1 Spatial distribution of water vapor

The air has only a limited storage capacity for water vapor, which depends strongly on the temperature of the atmosphere. Looking at the water vapor concentration of the RO measurements, one immediately sees that it follows a global pattern. The highest concentrations are found in the tropics, towards the poles the water vapor content decreases. At the poles, the concentration of water vapor is under 1% [Markings, 2017]. The water vapor concentration decreases not only with increasing latitudes, but also with the height. This is because the temperature decreases with increasing altitude and thus the air can not store as much water vapor.

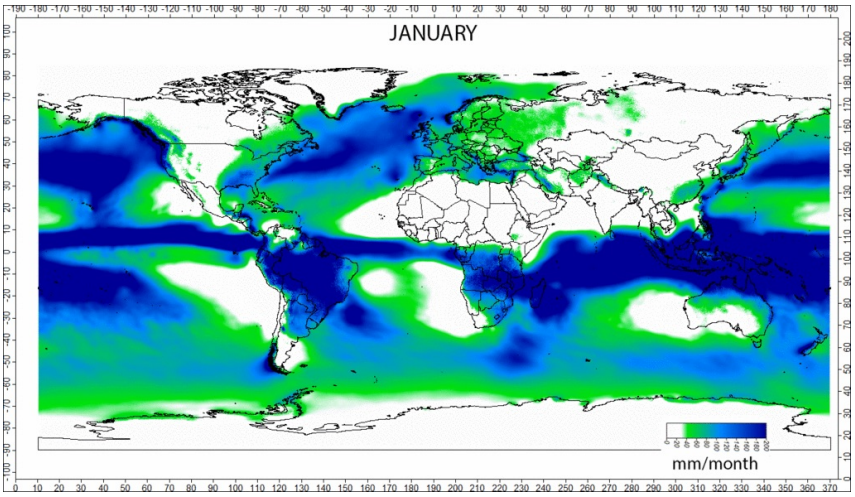

(a) Precipitation in January.

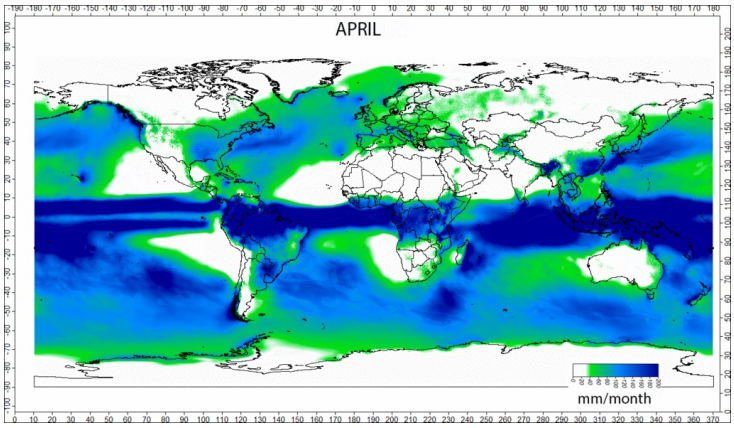

(b) Precipitation in April.

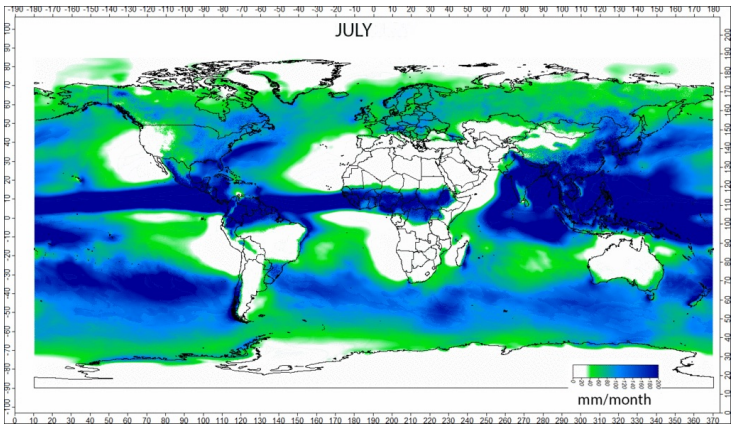

(c) Precipitation in July

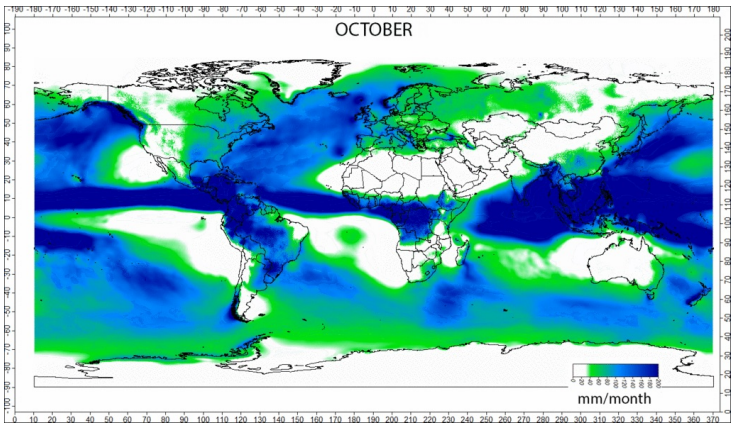

(d) Precipitation in October.

Figure 3: Distribution of water vapor between 1979 and 2013, which is given in [mm/month]. (Taken from Greenmind, 2016)

Figure 3 shows the water vapor content, during a year. In Figure 3 is the long term mean precitable water for the January, April, July and October from 1979 until 2013. In addition, it can be seen that the relative humidity over the oceans is higher than over land. This can be traced back to a higher evaporation rate over the oceans. The relationship between the evaporation and the surface temperature of the oceans can be described by the following equation [Gaffen et al., 1992].

$$ln(PW) = a + bT_s. \tag{2.7}$$

The equation shows that there is an exponential relationship between the surface temperature of the ocean T_s and the rate of the precipitable water, PW. Gaffen et al., 1992 analysed radiosonde data from 50 stations during 1973 and 1990, which were globally distributed and found out that the linear correlation coefficient between ln(PW) and T_s has a value of 0.94.
Further on, deviations from zone symmetry are related to the physiography of the Earth's surface.
Finally it is to mention, that the amount of rainfall over oceans is in general higher than over the continents.

2.3 Precipitation

Precipitation is the general term for all forms of moisture that originate from clouds and fall to the ground. It is that part of the water cycle in which atmospheric water vapor is condensed and forming water droplets that are so large, that gravity makes them fall to the earth.
The precipitation distribution looks similar to that of the atmospheric water vapor. About 66% of the total precipitation occurs in the equatorial region, more specifically between 30° north and 30° south latitude. Generally speaking, precipitation can not be grouped into zones, as it can vary widely. There are areas in which almost no precipitation falls, but elsewhere heavy precipitation can occur.
Extreme precipitation such as the global maximum in Cherrapunji, India, with more than 12 m per year, is always associated with advection and orographic effects [Liljequist and Cehak, 1984].
Precipitation plays also a special role in North America, because most precipitation is formed by water vapor from the warm waters of the Gulf of Mexico. Rainfall is transported deep into the interior of the country, providing rain in the United States.

Moist warm air from the Pacific can not penetrate far into the interior, as the Rocky Mountains run parallel to the coast and water vapor can not be transported across this mountain range. The same phenomenon can be observed in South America near the Andes.
On the east coast of the US, however, the deep penetration of water vapor into the interior is possible because there are no high levels of interference [Peixoto and Oort, 1992].

3 Atmospheric rivers

Atmospheric rivers are long, broad streams that can carry enormous amounts of water vapor. This water vapor gets transported by the AR from the tropics towards higher latitudes. The direction of the atmospheric rivers is influenced by the weather, especially by low pressure areas and storms.
These rivers can be 400 to 600 kilometers wide and up to 2000 kilometers long and are located in the lower part of the troposphere. Due to the extremely large amount of water vapor, this natural phenomenon can be very dangerous for people who live in the affected area. Atmospheric rivers can vary in length and width and are bound by no limits, except in height, as the water content in the atmosphere decreases with altitude.
This means that no event is the same as the other and therefore each is individual and unique. However, there are regions where this natural event occurs more often than in others. This can be explained by the particular geographical regions.
When an atmospheric river hits land, large-scale floods, landslides, overflowing rivers, and heavy precipitation in the form of rain or snow can be the consequences.
For this reason it is of great importance to be able to predict atmosperhic rivers and to know more about them. The following section explains the science behind the atmospheric rivers using as an example the United States of America (see subsection 3.3). [NOAA, 2015a]

3.1 Definition of an atmospheric river

For atmospheric rivers, there are a variety of definitions which have developed over time. In 1962 an atmospheric river was mentioned for the first time and so the first definition for an atmospheric river was introduced. The following table 3.1 gives an overview of the development of the definition of atmospheric rivers. The table is ordered chronologically, starting with the oldest definition, which was mentioned in a scientific paper.

Table 3.1: Definition of an atmospheric river

AR Definition	References
„characterized by strong gradients in a southwest flow of moist stable air from a rather distant low-latitude source, with a minimum of interruption by intrusion of air from a more northerly source“	(Weaver, 1962) (p. 207)
„water vapor transport in the troposphere is characterized by a filamentary structure“; „the fraction of the globe they cover is 10% or less“	Zhu et al., 1992, (Zhu and Newell, 1998)
„areas of strong winds (greater than 12.5 ms-1 wind speed [...]) with an Integrated Water Vapour (IWV) in the atmospheric column of more than 2 cm“	Zhu and Newell 1998, based on Newell and Zhu 1992
„quite narrow (<1000 km wide) relative to both their length scale (>2000 km) and to the width scale of the sensible component of heat transport“	(Neiman et al., 2008b)
„[Pineapple express] „steer warm, moist air from the tropics near Hawaii northeastward into California“	Dettinger 2011, based on Weaver 1962; Dettinger 2004
„they approach the west coast of North America, ARs are typically 2,000 or more kilometers long but only a few hundred kilometers wide“	(Dettinger, 2011)
„concentrate those fluxes into long (>2000 km), narrow (<1000 km) plumes“	Neiman et al. 2011, based on Bao et al. 2006; Stohl et al. 2008; Ralph et al. 2011
„narrow plumes of SSM/I vapor with values >2 cm that were >2,000 km long and <1,000 km wide“	(Dettinger, 2011)

„thousands of kilometers long and, on average, only 400 km wide“	Ralph and Dettinger 2012
„a contiguous region >2000 km in length and <1000 km in width containing IWV values >0 mm“	(Rutz and Steenburgh, 2012)
„long (>2000 km), narrow (<1000 km), low-level (below 600 hPa) plumes of enhanced water vapor flux“	Neiman et al. 2013, based on Zhu and Newell 1998; Ralph et al. 2004, 2005, 2011; Neiman et al. 2008a, b; Smith et al. 2010
„long (about 2000 km), narrow (about 300-500 km wide) bands of enhanced water vapor flux“	Gimeno et al. 2014 (p.1), based on Newell et al. 1992

3.2 Regions of atmospheric rivers

The beginning of atmospheric rivers is in the tropical regions, where warm, humid air is available. Local storms or cold fronts transport this air to the north, resulting in a stream of water vapor, which can transport the equivalent amount of water as the mouth of the Mississippi river, which discharges 16 792 m^3 of water per second into the Gulf of Mexico. [National Park Service, 2017]
If the atmospheric river hits land and there are mountains in the area, this can lead to extreme events. The humid air rises up the mountainside and condenses as the temperature decreases.
This effect will be discussed in the following chapter „The Pineapple Express 3.3“.
Atmospheric rivers can occur all over the world, but there are areas where this phenomenon is more common than in other regions. According to a new study, 300 million people are directly affected by floods and droughts every year. [NOAA, 2015a]
Furthermore, it was found that 22 percent of the total water that flows on the Earth's surface comes from atmospheric rivers. In some regions, such as the East and West coasts of the US, Southeast Asia or New Zealand, this amount may even exceed the 50 percent mark.
In areas where the influence of the atmospheric rivers is greatest, this value can be up to

80 percent. As a result more often extreme events occur, which can cause serious damage in the affected areas. The propability of floods or droughts increases to 80% and 90%, respectively, in these regions. Vice versa the absence of ARs can cause draughts. Should this happen the likelihood of droughts in this affected region increases by 90%.
Furthermore, atmospheric rivers also occur in Europe, in particular along the European Atlantic coast, the Iberian peninsula and in Scandinavia. [Ramos et al., 2016]
It was proven that eight of the ten heaviest precipitation events in Europe can be explained with atmospheric rivers. [Union, 2013] This number can be used to illustrate how important ARs are to Europe.
The event in December 2015 in the UK and Norway was one of the most devastating disasters triggered by an atmospheric river in Europe. Norway recorded the highest rainfall ever recorded in 24 hours during such an event.

Atmospheric rivers are distributed all over the world, but occur very frequently in California. In this region, they can be responsable for 30 to 50 percent of the rainfall.
There are some storms on the west coast of the US, but the most notorious storms are the so-called „pineapple express“storms. These storms bring warm humid air from the tropics over Hawaii (hence their name) to the American West Coast and can lead to heavy, torrential rainfalls in these places. Most of these Pineapple express storms occur between October and April and are therefore responsible for most winter storms. A feature of this atmospheric river is that even on simple satellite images they are recognizable as long, narrow cloud bands.[Dettinger, 2004]

3.3 Pineapple express

The pineapple express has its roots in the tropics and transports warm moist air masses across the Pacific Ocean to the west coast of the USA. On the way across the ocean, the water vapor conveyor reaches the area of the hawaiian islands. Therefore, the tropical name "Pineapple Express" originates from its geography. The pineapple express usually hits the east coast of the United States of America between 32° north and 52° north, mostly in the region at a latitude of 40°.

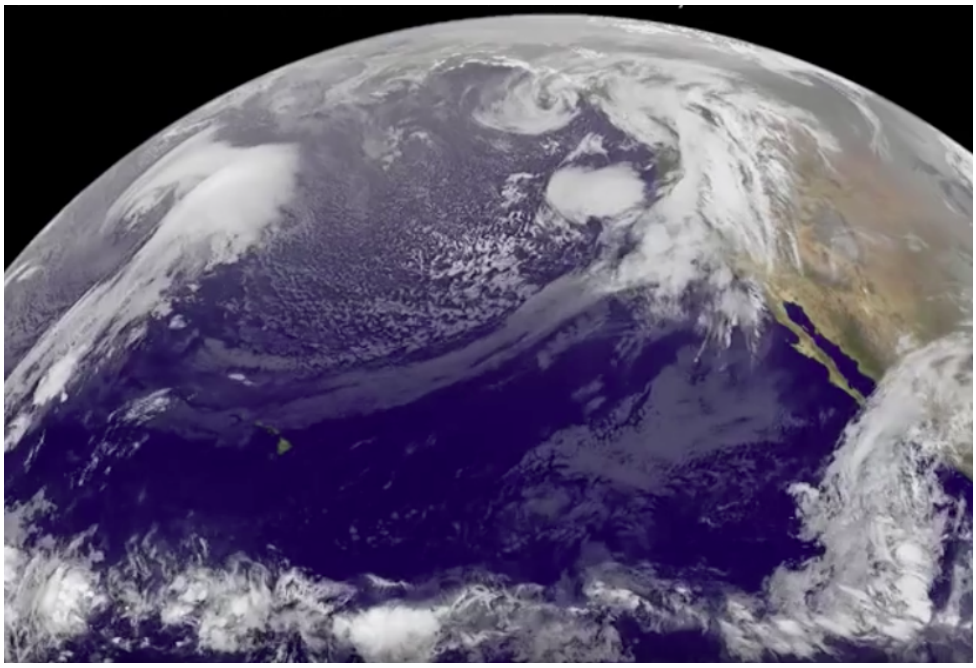

Figure 4: Satellite Image of a Pineapple Express. (Taken from Chesters, 2014)

Figure 4 shows a Satellite Image of an AR event, hitting the West Coast of the United States in December 2014. This AR is a type of the Pineapple Express, because the path of the water vapor band touches the islands of Hawaii.
When this wet air belt hits land, this usually happens in a very densely populated area, for this reason, this phenomenon enjoys a lot of attention and needs to be analysed to predict such events. The damage that can be caused by such an event reaches in some cases hundreds of millions Dollars.
To reach the American continent the AR has to travel for several thousand kilometres. When the AR is located over the ocean, no obstacle is in the way and the AR can spread in the direction, which is defined by the direction of wind and the actual weather conditions. When the AR hits the mainland of the United States, massive obstacles block the way for further travelling deeper into the country. The AR is blocked by the mountain chain of the Rocky Mountains. Some AR can travel over the mountain chain, but they are weakened by the obstacles.
As a result of the impact on the Rocky mountains, warm, humid masses of air rise up the mountainside, and undergo adiabatic cooling with increasing altitude. Moisture begins to condense with decreasing temperature and small water droplets form. A schematic example of the process is shown in figure 5.
The precipitation caused by these ARs can be very violent and devastating. In the years

from 1997 to 2006 it could be proven that each event of all 7 floods concerning the Russian river were caused by an AR in this time period. The heavy precipitation forces the Russian river in California to rise up to eleven meters, and thus overflow the shores and flood surrounding areas. The normal water level for the Russian river is 2 meters. [Dettinger and Ingram, 2013]

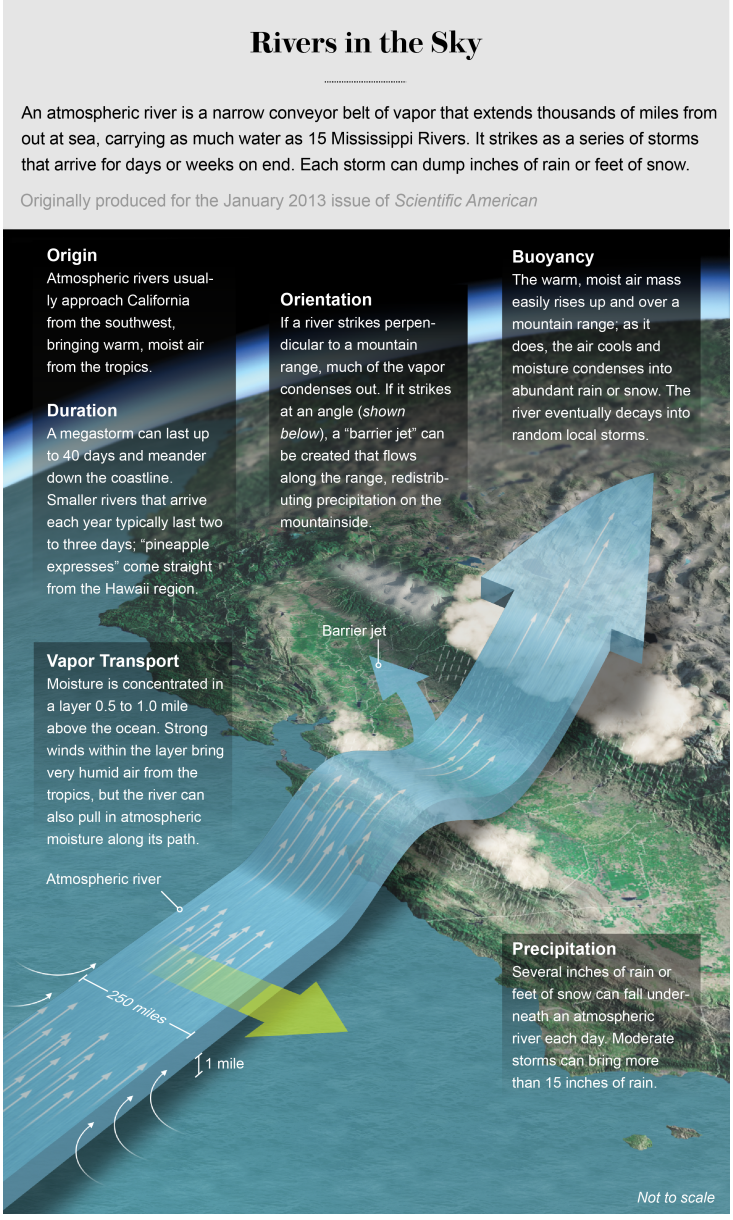

Figure 5: Schematic drawing of an AR, which hits the East coast of America. A barrier is drawn on the left side of the AR. (Taken from: Fischetti, 2018)

During winter the Pineapple Express storms carry twice as much water vapor in the Sierra Nevada as normal cold fronts, which can occur. Furthermore they yield to warmer minimum temperatures, and produce daily increases in streamflow that are an order of magnitude larger than those from other types of storms. Furthermore in the Sierra Nevada warmer minimum temperatures and an increase in the daily production of streamflow can be measured. [Dettinger, 2004]

A storm of extreme magnitude can rage for up to 40 days, causing severe damage. The amount of precipitation also depends on the direction of the atmospheric river. If a storm hits a mountain range vertically, most of the water vapor condenses and precipitation forms. However, if the impact angle does not correspond to 90°, a barrier jet can be formed. A barrier jet is a small tributary of the atmospheric river that flows along the mountainside, causing heavy rainfall in the affected area. A barrier jet is a relatively strong wind, which is concentrated within a narrow stream, on the windward side of a mountain chain. The barrier jet moves roughly parallel to the obstacle - in this case the Rocky mountains. The cold air ascends the barrier and as a result a pressure-gradient-force occurs, which points away from the mountains. (See figure 6) If this situation lasts longer as hours the Coriolis force, accelerates the stream in the perpendicular direction to the pressure gradient, which is along the barrier direction. [Seguin, 2012]

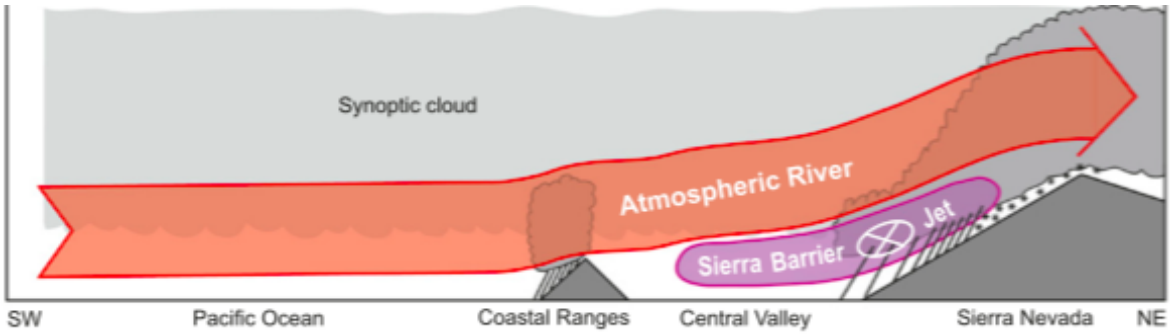

Figure 6: A schematic cross section through an AR event. (Taken from Neiman et al., 2013a)

3.4 Extrem events caused by atmospheric rivers

To give an overview of the destructive power of AR, the most documented serious events from the 1980's up to now are briefly summarized. The events are given in a chronologically order:

3.4.1 11 - 24 February 1986 Northern and Central California

- Event rainfall total of 49.6 inches at Bucks Lake in Feather River Basin
- Several rivers above flood stage.
- 13 fatalities, 67 injuries
- 50,000 people displaced by flooding
- $ 400 million in damages to property and infrastructure.

Leung and Qian, 2009

3.4.2 29 December - 4 January 1996/1997 Northern California and Western Virginia

- Event rainfall totals of more than 24 inches in many locations throughout northern California.
- Heavy rain at high elevations in the Sierra Nevada fell on top of deep snow pack exacerbated runoff and river flooding
- San Joaquin, Sacramento, Feather, Cosumnes, and Toulumne Rivers heavily impacted.
- 250 square miles inundated by flood waters
- 2 fatalities, 50 injuries
- 120,000 people displaced by flooding.
- $ 1.6 billion in damages; 20000 homes and 1500 businesses destroyed or damaged.
- Disaster areas declared in 43 counties in CA.

Leung and Qian, 2009, Galewsky and Sobel, 2005

3.4.3 7 - 11 January 2005 Southern California

- Event rainfall totals of 10 - 20+ inches throughout southern CA, with heaviest rainfall focused north and east of Los Angeles, CA.
- 14 fatalities, 9 injuries.
- Several hundred people displaced by flooding.
- $200?300 million in damages.
- Several structures destroyed by flash flooding
- Several road ways compromised by mudslides and flooding
- Major mudslide at La Conchita in Ventura County, CA, resulted in 10 fatalities and destroyed 15 homes

Ralph et al., 2011

3.4.4 13 - 14 2005 September Western Norway

- Rainfall total of 6.16 inches in 24 h at the Bergen-Florida weather, the most daily rainfall ever recorded at the site since observations began there.
- Rainfall total of 7.06 inches in 24 h at Opstveit, the most daily rainfall ever recorded in September in Norway.
- Landslides at Hatlestad Terrasse near Bergen caused 3 fatalities and 7 injuries and destroyed several homes, displacing several people
- Flooding and landslides caused severe damage to buildings and infrastructure around the city of Bergen.
- Strong winds downed powerlines and trees, adversely affecting communications and transportation.
  Stohl et al., 2008

3.4.5 29 December - 2 January 2005/2006 Northern California

- Event rainfall totals more than 20 inches throughout the Sierra Nevada.
- Locations in the Coastal Range in the Russian and Napa River basins received 18?30 inches.
- Widespread 24 h rainfall totals in excess of 5 inches on 31 Dec throughout Northern CA.
- Several rivers above flood stage throughout northern CA.
- Recurrence intervals for peak discharges throughout northern CA ranged from 10-25 years.
- Major flooding concentrated in Napa and Russian River basins.
- No fatalities reported.
- $300 million in damages.
- 10 counties declared federal disaster areas.
- 1000 homes were flooded in Napa, CA.
- Various local evacuations, road closures, slope failures (i.e., mudslides).

Smith et al., 2010

3.4.6 6 - 7 November 2006 Western Washington and Northern Oregon

- Event rainfall totals of 8 -20 inches over the Cascades and Coastal Mountains
- Local rainfall maxima near 28 inches in the Coastal Mountains and near 24 inches in the Cascades
- Several rivers above flood stage in western WA.
- Several stream gauges throughout the Coastal and Cascade mountain ranges in western WA and northern OR recorded 1-day discharges in the top 1% of those historically recorded, with 6 gauges reporting record discharges.
- No fatalities reported.

- $50 million in damages.
- Several roadways washed away by flood waters.
- Mudslides blocked roadways leading to road closures.

Neiman et al., 2008a

4 GNSS Radio Occultation

In order to detect atmospheric rivers, data with a high vertical and horizontal resolution available globally over Earth are required. There are several techniques for data collection, and each method has advantages as well as disadvantages for this application. Radiosonde measurement provides good quality data. However, with this method, the data sampling is limited, because it is only possible to perform the measurements on land.
Hence, Global Positioning System (GPS) radio occultation (RO) data are used, because of their global availability. RO data has a number of advantages over radiosonde measurements, such as long-term stability, all-weather capability and very high vertical resolution and accuracy. The measuring method is based on the principle of refraction. A GPS satellite sends an electromagnetic signal to a Low Earth Orbit (LEO) satellite [Steiner et al., 2011].The signal propagates through the Earth's atmosphere and is delayed and bent by it. How strong this effect is, depends entirely on the properties of the atmosphere. As a satellite enters occultation, the Earth's atmosphere is scanned from the ground up or vice versa. These events are called either setting occultations or rising occultations.The data quality, provided by the RO technique, is really good in the range from the upper troposphere (altitude of 5 km) to the lower stratosphere (altitude of 35 km).

4.1 RO measuring technique

Initially, the concept of the radio occultation measurement method was developed in the mid-sixties. The Mars and Venus atmosphere were measured using this measurement principle as part of the Mariner IV and Mariner V missions. The data obtained were a density and temperature profile of the two atmospheres [Fjeldbo et al., 1971]. Gradually, this concept was adapted to the Earth's atmosphere and was first tested on board the 1995 National Aeronautics and Space Administration (NASA) Microlab I spacecraft Global Positioning System / Meteorology (GPS / MET) mission.
Two satellites are brought into space which orbit the earth at a certain distance. The transmitter emits electromagnetic signals at a frequency of 1575.42MHz or 1227.60MHz, as this is the frequency of Global Positioning Satellites (GPS).
The transmitter is a satellite of the Global Navigation Satellite System (GNSS). GNSS includes the Global Positioning System (GPS) of the United States Department of Defense (DoD), the Global'naya Navigatsionnaya Sputnikovaya Sistema / Global Navigation Satellite System (GLONASS), operated by the Russian Vyska Vozdushno-Kosmicheskoy Oborony / Aerospace Defense Forces (VKO), GALILEO as a joint project of the European Union (EU) and the European Space Agency (ESA) and the Chinese BeiDou

satellite navigation system. The GPS and the GLONASS system are currently in operation, whereas the BeiDou and the Galileo system are currently still under construction or in partial operation. GALILEO and BeiDou are expected to achieve global coverage and full operational status by 2020. [Hayes, 2012]
Currently only GPS satellites are used for RO measurement, but theoretically it would be possible to use all satellites for the measurement method. There are currently 32 satellites in orbit around the Earth in the mid-Earth orbit (MEO) at an altitude of approximately 20,200 km with an inclination of 55 °, and for that four satellites are always visible from each point on the earth.
The radio signal propagates through the Earth's atmosphere and is refracted and delayed by the atmosphere's density gradient (see Fig. 7). A receiver, i.e. a LEO Satellite measures the phase change between the intrinsic signal and the frequency shifted signal as a function of time [Hajj et al., 2002]. This phase change measurements can be inverted to vertical profiles of atmospheric parameters (such as bending angle, density, temperature etc.).

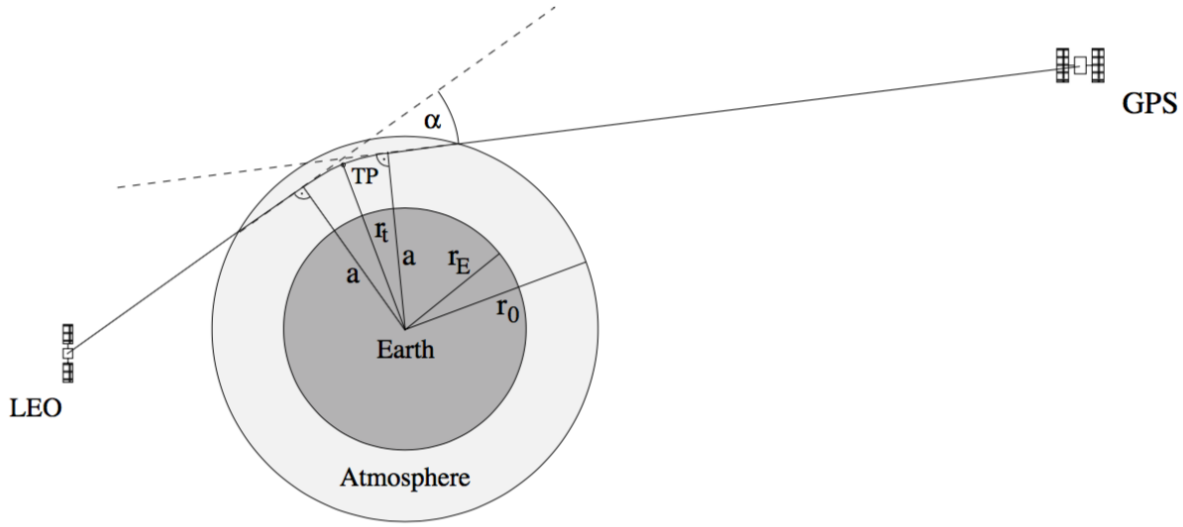

Figure 7: Schematic principle of RO. Within the influence of the Earth's atmosphere the signal between transmitter and receiver satellite is bent within the Earth's density field whereas above the atmosphere it does not undergo refraction. Taken from Foelsche, 1999.

The phase change is dependent on the electron density in the atmosphere, the content of the water vapor, the density and the temperature. A major impact on the bending angle profile is, that an ionospheric influence occurs. This effect can be removed with the

help of an ionospheric correction to first order. [Syndergaard, 2000] However, ionospheric residuals remain in the data. [Danzer et al., 2013]
The bending angle α is a function of the impact parameter a, which is the perpendicular distance between a ray asymptote and the refraction center (which is approximately in the center of the earth) and is constant along the ray path (see figure 7). At the point where the ray path is closest to Earth, a is given as n(r) r, where n is the refractive index and r is the radius of the ray path.

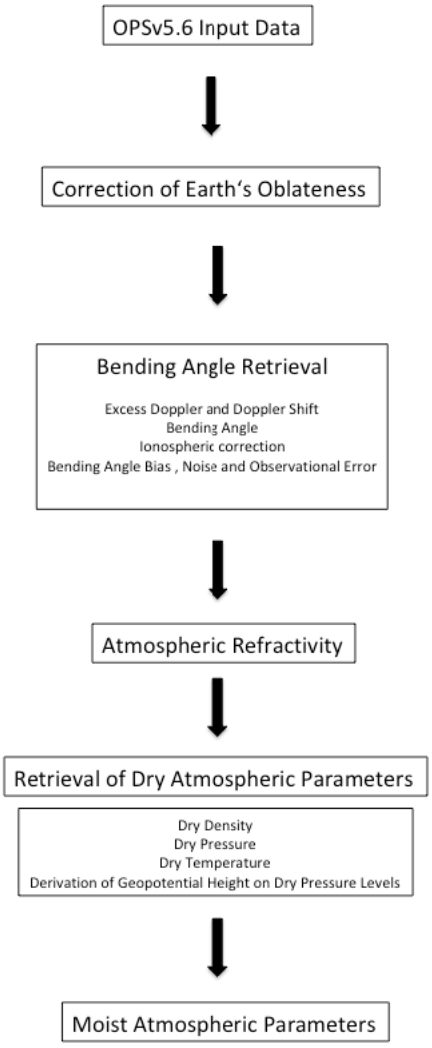

Figure 8: Scheme of the process for the retrieval of the moist atmospheric parameters. [Schwärz et al., 2013].

As the refractive index varies radially, the ray propagating through the atmosphere is refracted. The bending angle is obtained by integrating the bending angle along the ray path. Thus, bending angle profiles are converted by the Abel integral to refractive index profiles. The Abel integral is given for the bending angle α as:

$$\alpha(a) = \int_0^{\alpha} \mathrm{d}\alpha' = 2\mathrm{a} \int_{r=r_\mathrm{t}}^{r=\infty} \frac{1}{\sqrt{(nr)^2 - a^2}} \frac{dln(n)}{\mathrm{d}r} \mathrm{d}r, \tag{4.1}$$

with the impact parameter a, the radius of the tangent point $\mathrm{r_t}$, and the refractive index n [Kursinski et al., 1997].
In equation 4.1, the upper boundary of the integral is infinity. However the RO measurements are only available up to 80 km. For this reason an upper boundary has to be intitalized. The results of a bad initialization of the bending angle are errors in the refractivity profile. Further effects of bending angles at high altitudes are high noise, which also can be recognized by errors in the refractive profile. [Schwärz et al., 2013]
In order to obtain the refractive index from the bending angle, it is necessary to form the inversion of the integral (derivation from Steiner, 1998):

$$n(r_1) = \exp\left[-\frac{1}{\pi} \int_{a_1}^{\infty} \frac{\alpha(a)}{\sqrt{a^2 - a^2}} \mathrm{d}\alpha\right]. \tag{4.2}$$

Instead of using the refractive index n, it is common practice to specify the refractivity N, given by the following relationship:

$$N = (n-1) \cdot 10^6. \tag{4.3}$$

From refractivity atmospheric parameters can be derives by the Smith-Weintraub Formula, to first order.

$$N = 77.6 \frac{p_\mathrm{dry}}{T_\mathrm{dry}} + 3.73 \cdot 10^5 \frac{e}{T^2} - 4.03 \cdot 10^7 \frac{n_\mathrm{e}}{f^2} + 1.4W, \tag{4.4}$$

with the atmospheric pressure p in hPa, temperature T in K, partial pressure of water vapor e in hPa, electron density $\mathrm{n_e}$ in electrons $\mathrm{m^{-3}}$, transmitter frequency f in Hz, and the mass of liquid water content in the atmosphere W in g $\mathrm{m^{-3}}$.
The first term on the right side of equation 4.4 represents the hydrostatic dry term, the second term for the wet part, and the third term for the ionospheric part. The last part takes into account the proportion of liquid water in the atmosphere.

Since the proportion of liquid water in the atmosphere is very low and the ionospheric correction has already been applied to first order. Hence, the last two terms of 4.4 can be neglected.

Dry Air Retrieval:

If interested in the dry atmosphere, the moisture can be neglected, so term number 2 dissapears. Therefore, equation 4.4 is simplified to:

$$N = 77.6\frac{p_{\text{dry}}}{T_{\text{dry}}} = 77.6\rho_{\text{dry}}\frac{R^*}{M_{\text{dry}}}, \tag{4.5}$$

using the ideal gas law, where $R^* = 8.3145$ J/(K mol) is the universal gas constant [Mohr et al., 2008] and M = 28.964 kg kmol^{-1} is the mean molar mass of dry air [Khélifa et al., 2007]. The dry density can be calculated as follows:

$$\rho(z)_{\text{dry}} = N(z)\frac{M}{77.6R}. \tag{4.6}$$

Once the density is calculated the pressure can be obtained from the hydrostatic equation given by:

$$p(z) = \int_z^\infty g(\phi, z')\rho(z')dz'. \tag{4.7}$$

The pressure equals the weight of the air column, which lays over an area. The upper boundary of the integral, which is theoretically infinity, is set to 120km (background information) [Schwärz et al., 2013]. As a final step, inserting density and pressure into the ideal gas law yields the dry temperature:

$$T(z) = \frac{M}{R^*}\frac{p(z)}{\rho(z)}. \tag{4.8}$$

To reduce noise, a Blackman filter is applied with 1 km filter width, to eliminate the numerical noise. Because of the chosen filter width, the resolution is not degraded [Schwärz et al., 2013]. A result of the calculation is, that the temperature does not decrease exponentially with height. The minimum temperature can be found at the tropopause, which is in a height of approximately 10 km. After the tropopause the dry temperature increases again, because of the availability of ozone. (see figure 9)

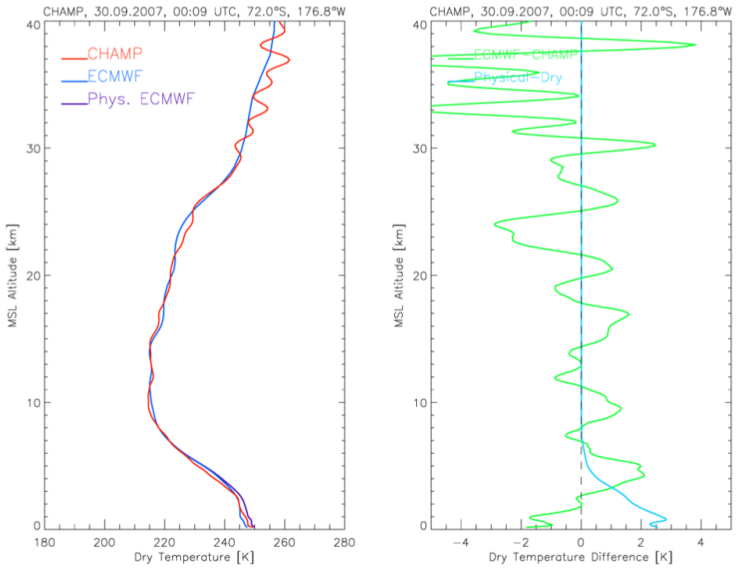

Figure 9: Comparison of dry temperature profiles of RO and ECMWF and ECMWF physical temperature as a function of height. (Taken from Schwärz et al., 2013)

Moist Air Retrieval:

Once the dry parameters have been derived, the wet parameters can be calculated:

$$N = c_1 R_\mathrm{d} \rho_\mathrm{dry} = c_1 \cdot \frac{p_\mathrm{dry}}{T_\mathrm{dry}}, \tag{4.9}$$

which represents the relation of dry air to refractivity. Equation 4.9 contains the dry air equation of the state $\frac{p_\mathrm{dry}}{\rho_\mathrm{dry}} = \mathrm{R_{dry}T_{dry}}$, where $\mathrm{R_{dry}} = \frac{R^*}{M_\mathrm{dry}}$ is the specific gas constant of the dry air. 4.9 makes it possible to formulate the ratio of dry pressure $\mathrm{p_{dry}}$ and dry temperature $\mathrm{T_{dry}}$ with respect to generic refractivity,

$$c_1 \frac{p_\mathrm{dry}}{T_\mathrm{dry}} = N(T, V_\mathrm{w}, p). \tag{4.10}$$

The water vapor volume mixing ratio $\mathrm{V_w}$ incorporates the water vapor pressure e, as well as the pressure p and the specific humidity q, as follows

$$V_\mathrm{w} = \frac{q}{a_\mathrm{w} + b_\mathrm{w} q}, \tag{4.11}$$

$$q = \frac{a_{\mathrm{w}} V_{\mathrm{w}}}{q + b_{\mathrm{w}} V_{\mathrm{w}}}, \tag{4.12}$$

where $a_w = M_w/M = 0.6220$ and $b_w = 1$ - $M_w/M = 0.3780$ are constants, where M_w is the molecular weight of water $M_w = 18.0153$ kg kmol^{-1} . The R.H.S. of Eq. 4.10 refers in principle to any existing type of refractive relationship [Foelsche, 1999, Smith and Weintraub, 1953].
With help of the Smith-Weintraub formula,

$$N = c_1 \frac{p}{T} + c_2 \frac{e}{T^2}, \tag{4.13}$$

the R.H.S. of Eq. 4.10, N, can be rewritten as

$$N(T, V_{\mathrm{w}}, p) = N = c_1 \frac{p}{T} \left(1 + \frac{c_{\mathrm{T}}}{T} V_{\mathrm{w}}\right), \tag{4.14}$$

where $c_T = c_2/c_1$. Three equivalent forms can be written:

$$T = T_{\mathrm{dry}} \frac{p}{p_{\mathrm{dry}}} \left(1 + \frac{c_{\mathrm{T}}}{T} V_{\mathrm{w}}\right), \tag{4.15}$$

$$V_{\mathrm{w}} = \frac{\frac{p_{\mathrm{dry}}}{p} T - T_{\mathrm{dry}}}{\frac{c_{\mathrm{T}}}{T} T_{\mathrm{dry}}}, \tag{4.16}$$

$$p = p_{\mathrm{dry}} \frac{T}{T_{\mathrm{dry}} \left(1 + \frac{c_{\mathrm{T}}}{T} V_{\mathrm{w}}\right)}, \tag{4.17}$$

Comparing the logarithmic values of dry pressure and pressure, the moist pressure vertical increment dlnp with respect to the dry pressure increment can be expressed as follows:

$$\frac{\mathrm{d} \ln p}{\mathrm{d} \ln p_{\mathrm{dry}}} = \frac{R_{\mathrm{d}} T_{\mathrm{dry}}}{R_{\mathrm{d}} T (1 + c_{\mathrm{w}} q)}, \tag{4.18}$$

and further on

$$\mathrm{d} \ln p = \mathrm{d} \ln p_{\mathrm{dry}} \frac{T_{\mathrm{dry}}}{T(1 + c_{\mathrm{w}} q)}. \tag{4.19}$$

With help of Eq. 4.12 q can be converted to V_w,

$$1 + c_w q = 1 + \frac{b_w V_w}{1 + b_w V_w} = \frac{1 + 2b_w V_w}{1 + b_w V_w}, \tag{4.20}$$

the result is

$$\mathrm{d} \ln p = \frac{T_{dry}(1 + b_w V_w)}{T(1 + 2b_w V_w)} \ \mathrm{d} \ln p_{dry}. \tag{4.21}$$

If q is given, the temperature T as well as the pressure p can be calculated. Further on V_w and p can be calculated, if T is given.

As starting values for the iteration process for the calculation of T, p and V_w the following parameters are used:

- $T_0 = T_{dry}$
- $V_{w0} = \frac{q_{minE}}{a_w}$; $q_{minE} = 1.51^{-6}$ g kg^{-1}
- $p_0 = p_{dry}$

Finally, after the iteration process, optimally estimated T and q profiles are obtained. The profile of the water vapor e is calculated as:

$$e = V_w p, \tag{4.22}$$

The density profile ρ is computed by the following equation:

$$\rho = \frac{p}{R_d T(1 + C_w q)}. \tag{4.23}$$

In the following figure 10, the pressure profile is shown and an exponential decrease with

altitude can be recognized.

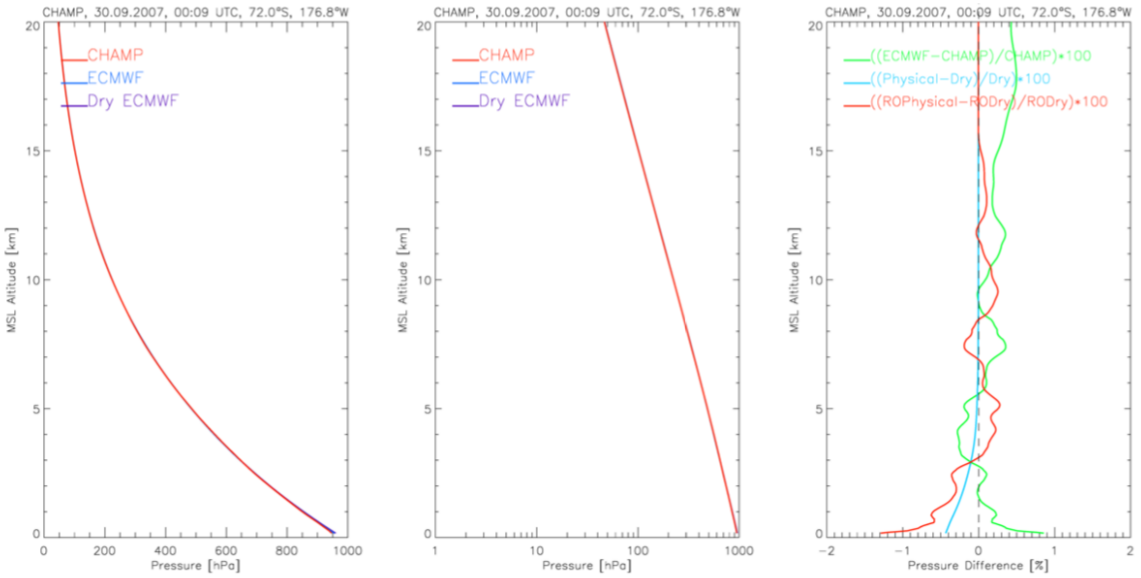

Figure 10: Comparison of moist pressure profiles of RO and ECMWF physical pressure and ECMWF dry pressure as a function of height. (Taken from [Schwärz et al., 2013])

4.2 RO characteristics

Vertical and horizontal resolution:

The RO measurement method achieves a very good vertical resolution. However, the horizontal resolution during one satellite circulation is low. The horizontal resolution becomes better, when the satellites cover the earth during time. The resolution in the lower troposphere reaches about 60 km horizontally and 100 m vertically in the lower troposphere. The horizontal as well as the vertical resolution of the measurement in the lower stratosphere is about 300 km and 1.5 km. [Kursinski et al., 1997, Gorbunov et al., 2004, Melbourne et al., 1994]. However, with the help of wave optics into the retrieval, a vertical resolution of 60 meters can be achieved.

Global coverage:

The location of the measurement is determined on the one hand by the orbit of the transmitter, as well as, by the receiver satellite. Most RO satellite missions

have a near-polar orbit for global coverage. However, GPS satellites have a fixed inclination of 55 °. The International Radio Occultation Working Group recommends at least 20 000 occultations measurements per day. Furthermore they emphasize the need for global coverage as well as coverage of all local times. The global coverage for the 13th Ocotber, 2009, can be seen at figure 11.

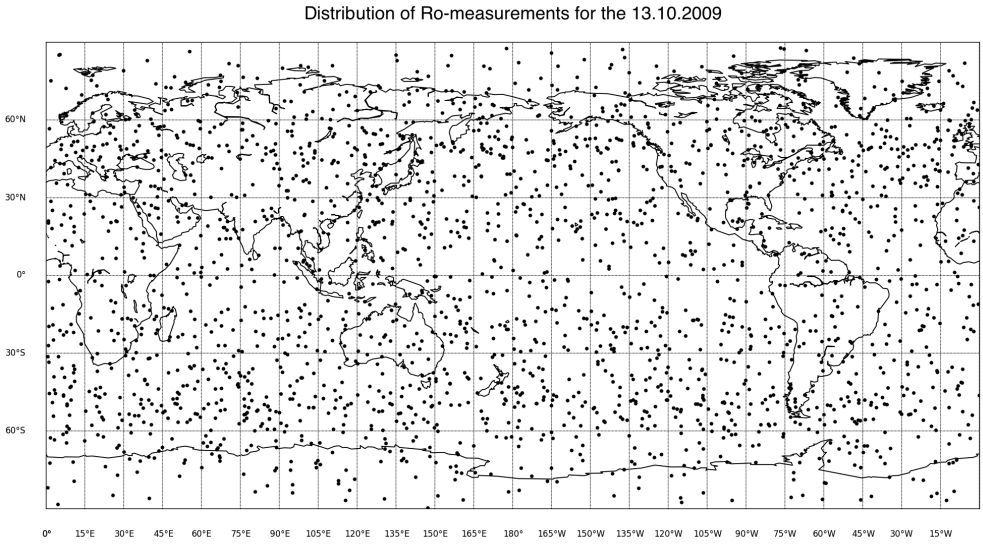

Figure 11: Distribution of RO - measurements for the 13th October, 2009.

All-weather capability:

A big advantage of the RO measurement method is that it can be used in all weather conditions. This is because GNSS signals can penetrate almost all clouds and are not disturbed by sunlight. That means that measurements can be made during the day as well as at night. It can happen that a large amount of water vapor in the atmosphere leads to disruption and signal degradation as a result [Gorbunov et al., 2000].

Self-calibration, long-term stability:

The measured quantity onboard a LEO satellite is the phase change as a function of time between the intrinsically transmitted signal and the received frequency-shifted signal. Assuming that the atmosphere does not undergo

major changes during the measurement of a profile, the RO technique can be called self-calibrating. This also implies that the measurements are long-term stable, which allows to use measurements taken by different LEO satellites without the need of inter-calibration [Foelsche et al., 2011].

Accuracy:

Accuracy of RO data depends on several parameters [Kursinski et al., 1997]:

- quality of the instrument
- ionospheric conditions
- atmospheric conditions (WV ambiguity, atmospheric multipath)
- quality of the initialization of the Abel integral

In the Upper Troposphere - Lower Stratosphere (UTLS) region, temperature errors rarely reach 1 K [Kursinski et al., 1997].

5 Data Sets

In this work, data was used, which was calculated using the Wegener Center occultation processing system version 5.6 (OPSv5.6). Specifically, data from the FORMOSAT-3 / COSMIC mission was used. Data which can be received from the RO data are pressure, density, temperature, Geopotential Height (GPH), and the water vapor. The exact derivation of the parameters was explained in chapter 4.1. The profiles of the parameters are a function of pressure. The vertical levels of the pressure grid can be calculated as follows:

$$p(z) = p_0 exp(\frac{z}{H}), \tag{5.1}$$

with p0 = 1013.25 hPa (standard surface pressure), H = 7000 m (constant scale height), and altitude z ranging from the surface to 16km (corresponding to about 100 hPa) in equidistant 200 m steps.
The highest accuracy of the data can be found in the upper troposphere, where there is a temperature of 0.7 K and a geoid height of 10 m. [Scherllin-Pirscher et al., 2011]
Because the RO measurement data is randomly distributed, a grid of 2.5 x 2.5 degrees is spanned over the Earth and a weighted average (see Eq.: 5.2) in space and time is applied to the measurement results. The formula for the weighted average is as follows:

$$x_{\text{grid}} = \frac{\sum\limits_i w_{\text{i}} x_{\text{i}}(\lambda', \Phi', d')}{\sum\limits_i w_{\text{i}}}, \tag{5.2}$$

where $x_{\text{grid}}(\lambda, \Phi, d)$ is a specific grid cell at longitude λ, latitude Φ, and day d. $xi(\lambda', \Phi', d')$ denotes an individual atmospheric profile at the RO event location (λ', Φ') and day (d'). It is to mention, that all RO measurements, within $\pm 7.5°$ in latitude and $\pm 2°$ in longitude are in the calculation considered. Further on every RO event within 2 days is also included. The weighting function is a gaussian function, which can be written as:

$$\omega_{\text{i}} = exp\left(-\left[\left(\frac{\Delta\lambda}{L}\right)^2 + \left(\frac{\Delta d}{D}\right)^2\right]\right) \tag{5.3}$$

where $\Delta d = d - d'$, $\Delta\lambda = \lambda - \lambda'$, L = 7.5° and D = 1 day. This resolution was chosen, because of the minimisation of the number of empty grid cells. [Brunner et al., 2016]

5.1 RO missions

Initial RO measurements were first delivered in 1995 by the GPS / MET mission [Ware et al., 1996]. Following on, more satellite missions were launched such as the Challenging Mini-Satellite Payload (CHAMP) mission. In this work, we use data from the so-called COSMIC mission.

This was one of the most important satellite missions over time, which was successfully launched on April 15, 2006 by Vanderberg Air Force Station in California and placed in an orbit of 516 km altitude. The FORMOSAT-3 / COSMIC (China Satellite-3 / Constellation Observation System for Meteorology, Ionosphere and Climate) is an international collaborative project between the NSPO (National Space Program Office) of Taiwan and UCAR (University Corporation for Atmospheric Research) of the United States of America. Launched in December 1997, the project will launch a LEO constellation of six microsatellites to collect atmospheric remote sensing data for operational weather forecasting, climate, ionospheric (space weather monitoring) and geodesy research. [Kramer, 2002]

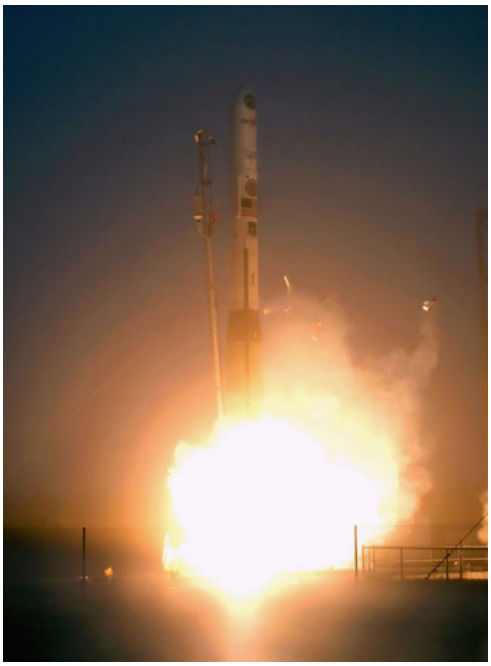

Figure 12: Launch of the Formosat 3 satellite in Vandenberg in 2006. Source: [UCAR, 2017]

About 1,600 to 2,400 atmospheric and ionospheric probes per day can be performed on this mission. The results of these measurements are vertical profiles that include temper-

ature, pressure, density, water vapor, and electron density of the atmosphere.
It should also be noted that these vertical profiles can be measured around the globe including the oceans [Anthes et al., 2000], to make more accurate predictions. Furthermore, these measurements also play an important role in Numerical Weather Prediction (NWP) and the prediction of typhoons, hurricanes and cyclones. [Anthes et al., 2008].
The results of these investigations showed that the mission delivered much better and more accurate results than previous missions. In the near future, a variety of satellite missions could be used to expand RO technology and achieve even better coverage [Kuo et al., 2004,Anthes et al., 2008]. In summary, the great success of this RO mission ushered in a new era of real-time RO method transfer. [Kuo et al., 2004]

6 Results

This chapter presents the results, which were achieved in this master thesis. Four AR events were chosen and analysed in reference to height distribution as well as to the development of the AR in the affected areas. The four selected events are:

1. 2006 western Washington and northern Oregon
2. 2009 Northern and central California
3. 2015 Great Britain
4. 2015 Norway

Each event is shown in a time series of plots, representing the integrated water vapor, which is plotted over a map. So, the AR can be detected and tracked during its travel path over the affected regions. Further on, some informations about the extent of the damage for every AR in the affected area are given.

6.1 2006 western Washington and northern Oregon

In 2006, an atmospheric river influenced West Washington and North Oregon. A maximum precipitation of 71 mm in the coastal mountain and 61 mm in the Cascades (mountain chain in California) could be measured. The results were violent floods and landslides, which blocked various roads. Several measurements were carried out of the event, which registered an absolute precipitation of the highest 1% of the measurements ever recorded. The damages in these regions were estimated to be around USD 50 million and higher. [Fears, 2015], [.Neiman et al., 2011]
The used data for this calculation were concentrated on ten days around the event. So the observation period starts on the 2^{th} November 2006 and ends on the 11^{th} November 2006. As a result the calculated precipitable water was plotted over the entire Earth, to recognise the AR and show the vast impact of the phenomena on the affected area. If we have a look at the plotted results of the calculations over time, the AR can be detected very well. To make the AR even more visible, a smaller section with a latitude of 5° to 65° and a longitude of 120° east to 150° west degrees was selected. Furthermore the color scale has been chosen differently, so that above a value of 25 mm, the values are marked in dark red and the AR can be clearly recognised.

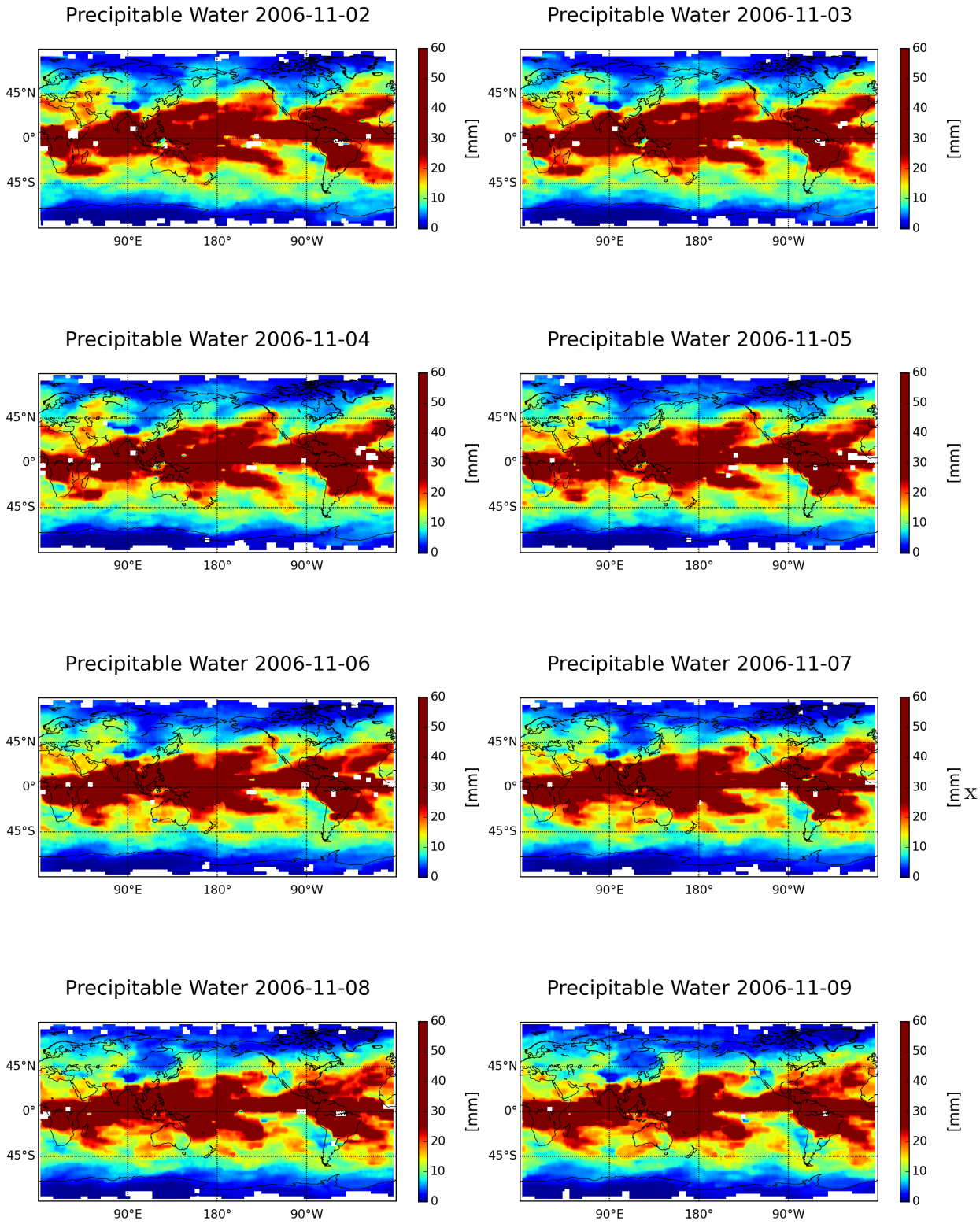
Precipitable Water 2006-11-02
Precipitable Water 2006-11-03
Precipitable Water 2006-11-04
Precipitable Water 2006-11-05
Precipitable Water 2006-11-06
Precipitable Water 2006-11-07
Precipitable Water 2006-11-08
Precipitable Water 2006-11-09
45°N
0°
45°S
90°E
180°
90°W
[mm]
0
10
20
30
40
50
60

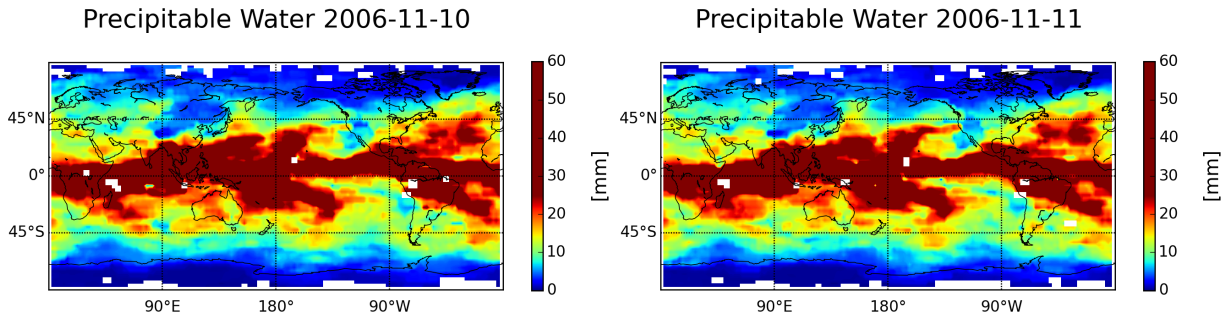

Figure 13: Plot of the precitiable water over the entire Earth in November 2006. An AR is detectable on the east coast of the United States of America.

The previous plots in figure 13 show the precipitation distribution over the world. Because of the loss of details at this kind of view, it is very difficult to detect the AR in Washington. To emphasise the AR better, the area of interest is zoomed in (figure 14) and the colorbar is transformed as explained above.

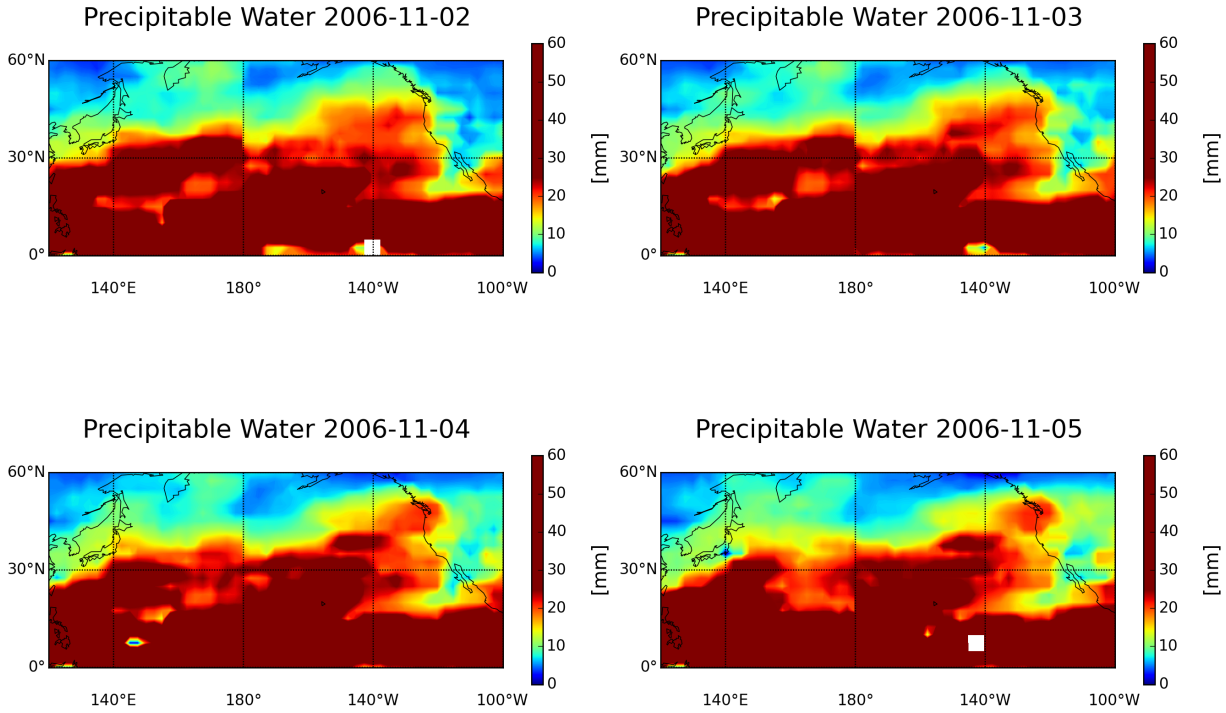

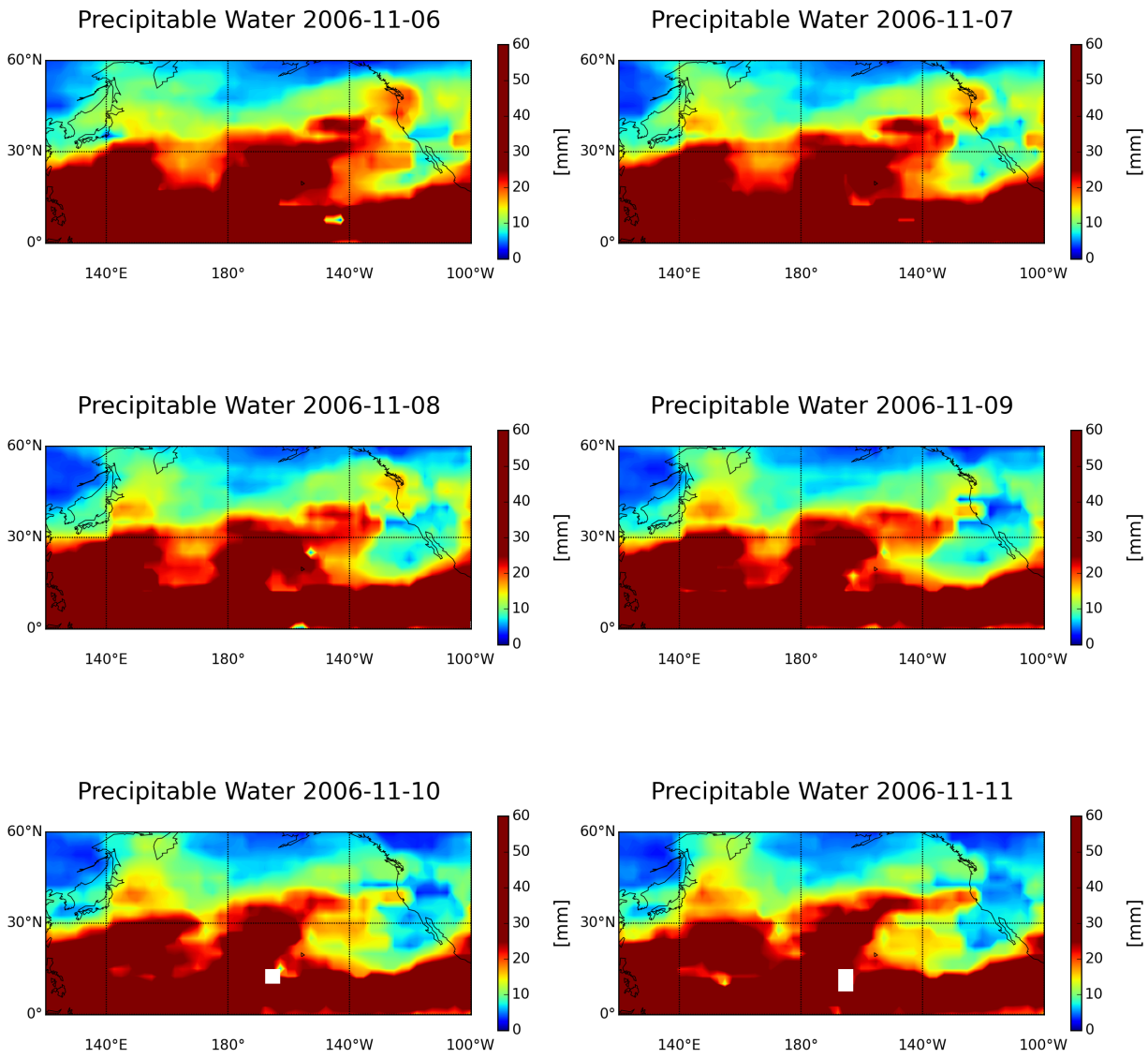

Figure 14: The event in 2006 is zoomed in to recognize the AR better. On the 5th and 6th November the highest precipitable water was calculated on the east coast of the United States.

The AR heads to the shore and develops like a wall which travels over the ocean and brings massive precipitation in form of rain- and snowfall. On 4th November 2009 the first harbingers of the AR hit the west coast of the United States of America. At the 6th and 7th November heavy rainfall destroyed parts of the affected regions. From 8th November the AR begins to collapse and the precipitation gradually stops.

In the next chapter the height distribution of the event is discussed, where an affected region is chosen and the average of the moisture for every height layer is calculated.

6.2 Height distribution - 2006 western Washington and northern Oregon

The vertical distribution of ARs is one of the main features of an event. This distribution gives information about how high an event extends and in which height the most moisture can be found. This perspective gives a closer look on an AR event, which is important, because no event resemble one another. Some AR have a lower elevation and extend only up to 2500m in height.
First of all, the distribution of moisture has to be calculated by the arithmetic mean for the selected area of each altitude layer. All measurements in a specific height layer are summed up and then divided by the amount of measurements in each height layer. So, the result is a single value for each layer, which represents the amount of water in the air. Afterwards the arithmetic mean is plotted over the time period, where an event took place. With reference to the AR in western Washington and northern Oregon the time axis is scaled from the 2nd November to the 11th November. The height is scaled from 0 to 5000 meters and consists of 25 values, which means that the vertical resolution is about 200 meters.
The size of the area, where the arithmetic mean is calculated can vary from event to event, because the affected area of every AR is different. At this case, an area of 7.5 x 7.5 degrees is selected, which refers to the coastal zone of impact. The selected area is mapped at the following figure (figure 15).

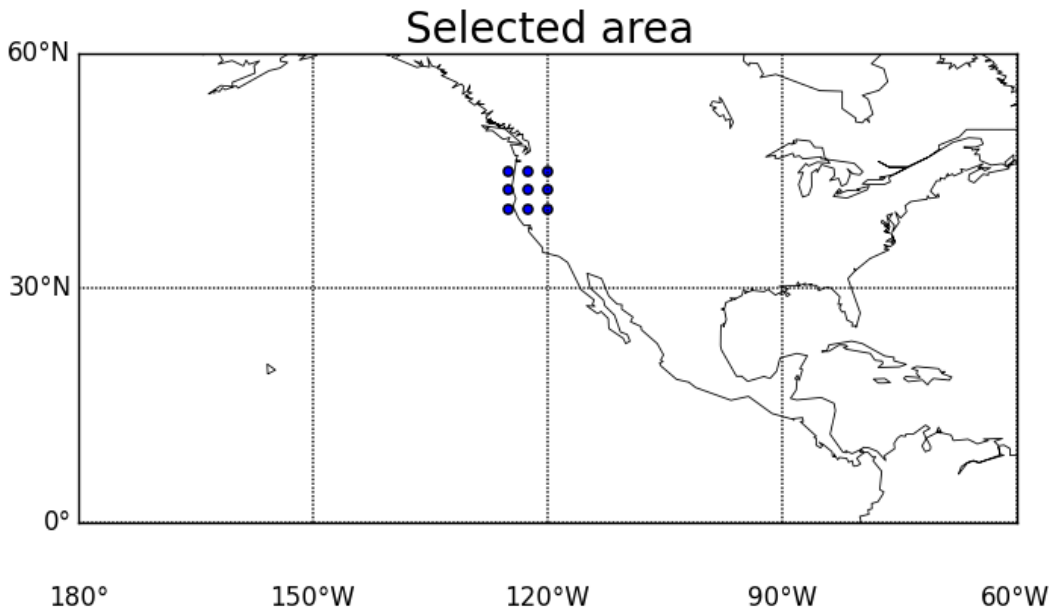

Figure 15: Map of the affected area, with the 7.5° x 7.5° grid for the arithmetic mean calculations.

Fig 16, shows the the vertical extent of the AR developing in time. The plot indicates the event reaches its peak between 04.11.2006 and 08.11.2006. During this period, the highest humidity values are reached at a height of approximately 2500 m.

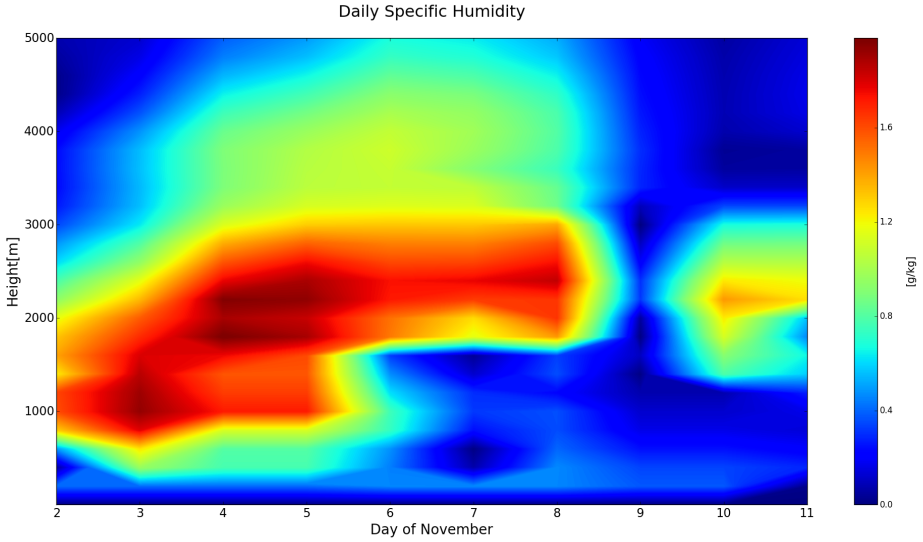

Figure 16: Height distribution of water vapor during the AR in November 2009 affecting the East Coast of the United States.

The AR builds up, and the amount of water vapour in the air rises. On the 2nd November the most amount of water vapour can be found under 2000 meter. Until the 4th November the biggest proportion of water vapour reached 4000 meter. This limit of 4000 meter remained the upper boarder during the event. On 09.11.2006 the AR decays and the specific humidity drops to a value of approximately 0.4 g / kg. Further on, the AR event begins to build up at around 800m, reaching up to an altitude of about 1800m, during this specific event.
Finally it is to mention, that this event was an AR from the type of a „Pineapple Express“, which was discussed in chapter 3.3.

6.3 2009 northern and central California

A further event of an AR, which was investigated, is a event in 2009, which hit northern and central California. The average amount of rainfall, which was caused by the atmospheric river on 13th to 14th October, is significant. During this event, a maximum precipitation of 48.26 mm was measured. The result of the heavy rainfalls were landslides in the coastal Santa Cruz Mountains and Sequoia National Park in the Sierra Nevada. The damage was estimated to $ 10 million. [Ralph et al., 2011].
To analyse this event, a time series of ten days was used, starting with the 9th October 2009 and ending with the 18th October 2009. In figure 17, ten plots are shown, with the results of the precipitable water. If the calculated result is higher than a value of 25 millimetres, the color is dark red to show the AR event. [Behrangi et al., 2016]

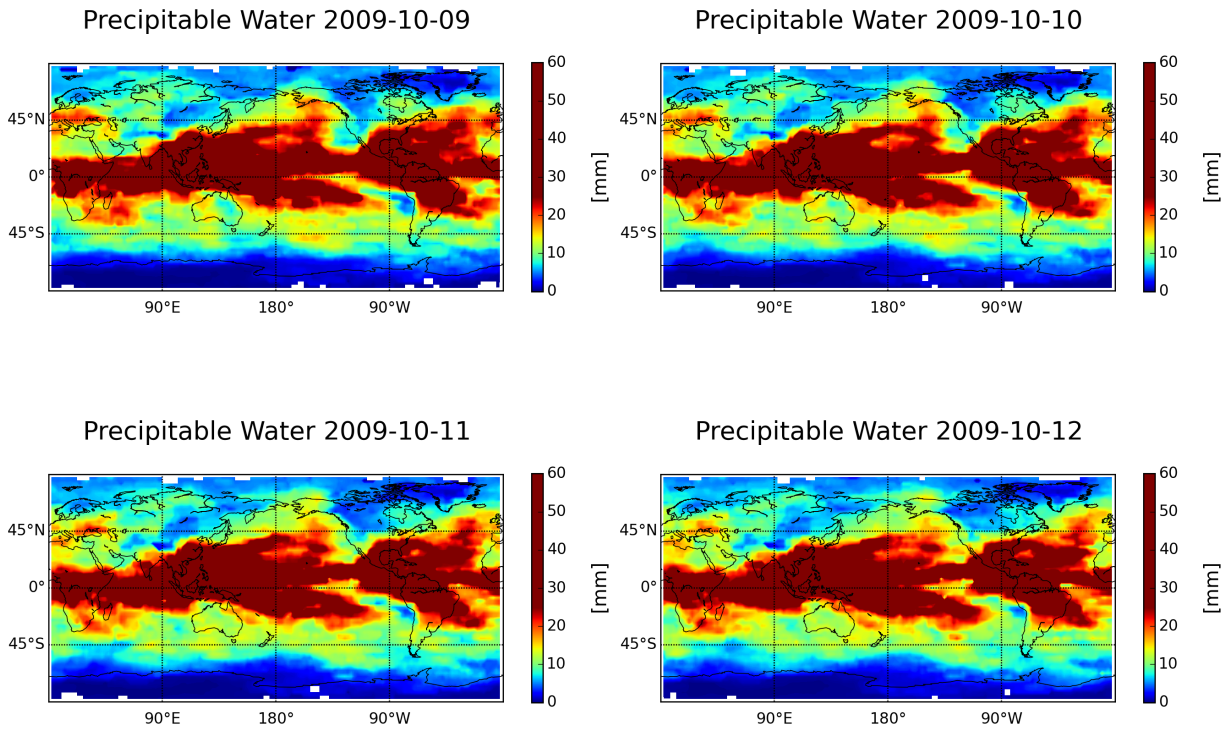

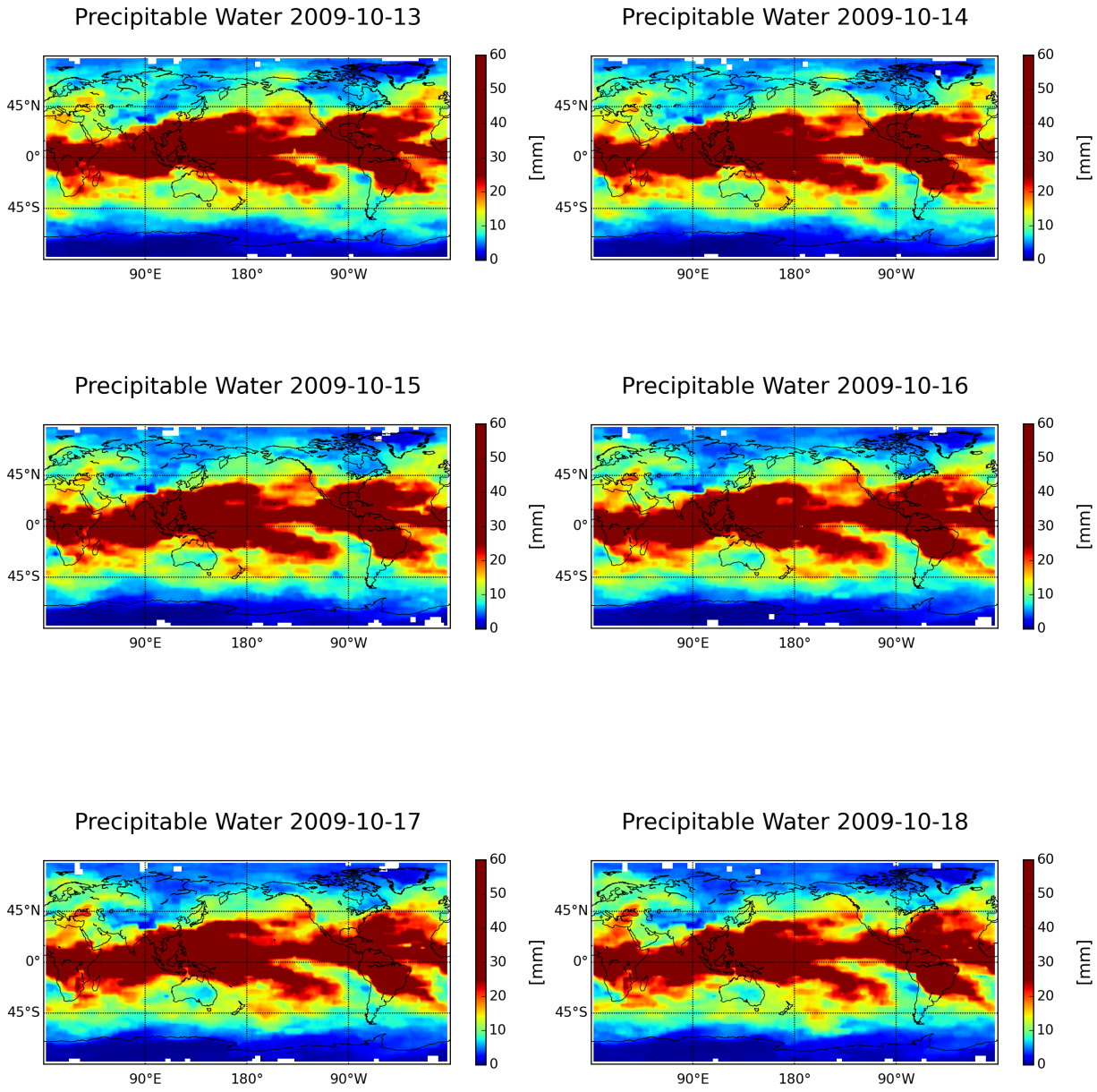

Figure 17: The AR event in 2009 which hit the East coast of the United States of America.

At the 13th October 2009 the AR reaches the west coast, where a precipitation over 25 mm is calculated. In the plots, a high concentration of water in the atmosphere over the affected area can be recognized until the 18th October 2009. To make the AR more visible a smaller area is chosen and the results are shown in figure 18.

Precipitable Water 2009-10-09

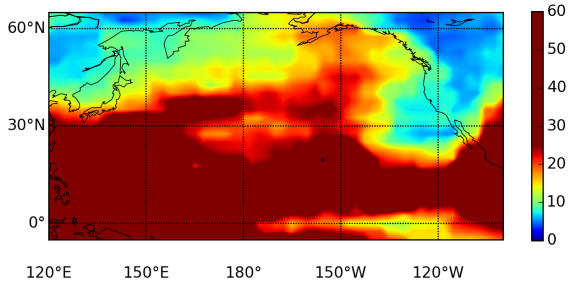

Precipitable Water 2009-10-10

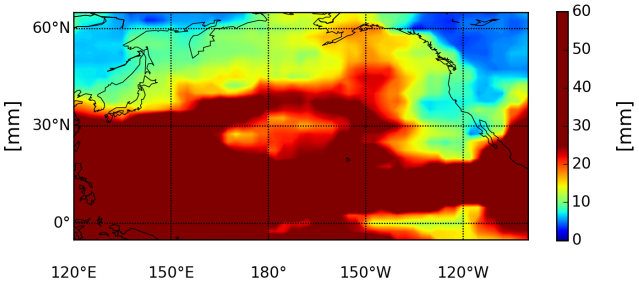

Precipitable Water 2009-10-11

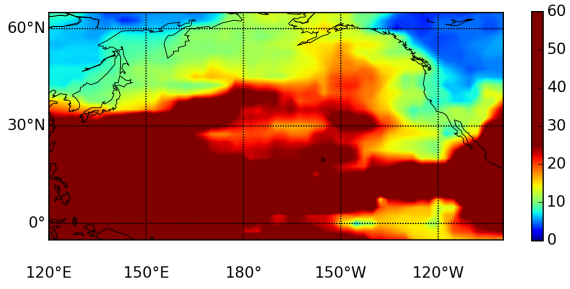

Precipitable Water 2009-10-12

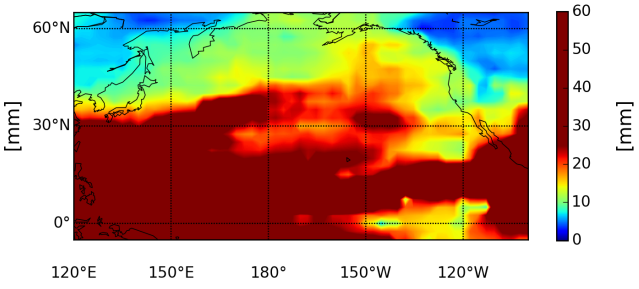

Precipitable Water 2009-10-13

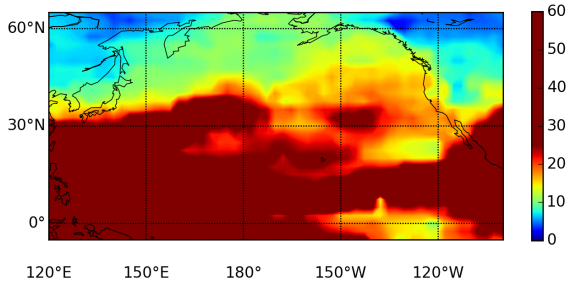

Precipitable Water 2009-10-14

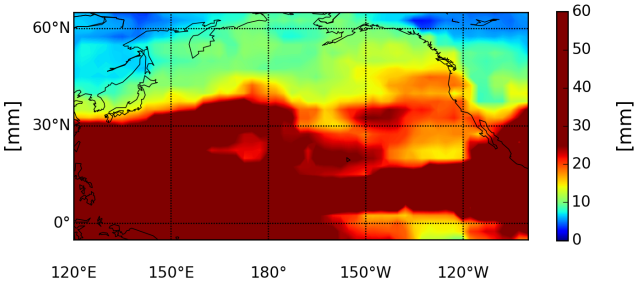

Precipitable Water 2009-10-15

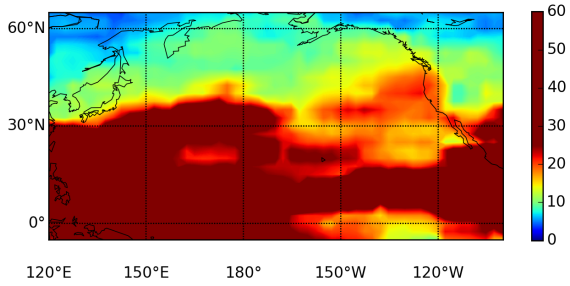

Precipitable Water 2009-10-16

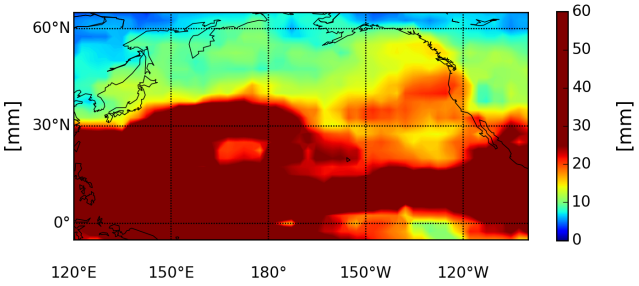

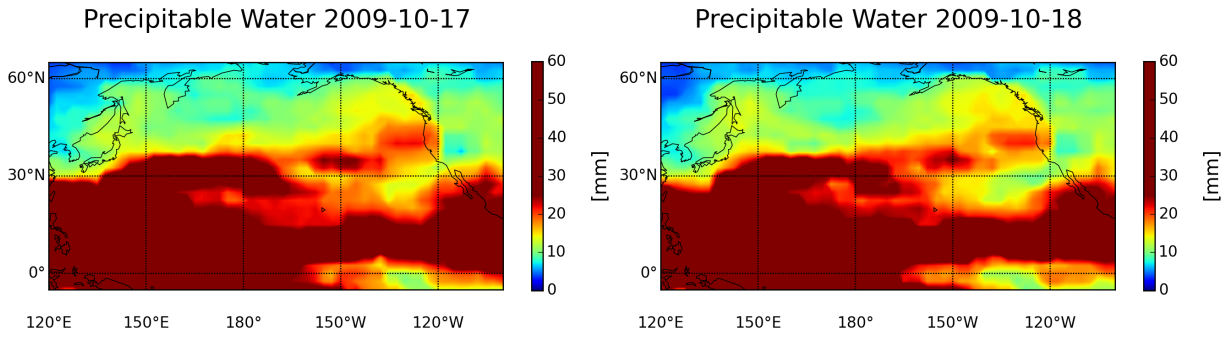

Figure 18: The AR event in 2009 which hit the East coast of the United States of America.

To analyze the AR better, the height distribution will be discussed in the following section.

6.4 Height distribution - 2009 northern and central California

At this event in northern and central California in 2009, the altitude distribution of water vapor is very different from the previous event. Again, an area with a 7.5° x 7.5° grid was selected, where the average of the water vapour was calculated for each altitude level. This region is limited by Seattle to the north and by the San Francisco area to the south. From the 9th to the 11th of October 2009 the first cloud front hit the coast, which can be seen in Fig. 18 and Fig. 20, which is representing the height distribution of the water vapor plotted over time. On the 13th October 2009, the AR met ashore, which lead to extreme precipitation.

The concentration of water vapour reached up to 3 g/ kg, which was recorded at an altitude of approximately 900 meters. The upper boarder of the AR was around 3700m of height. Hence, this event did not reach the same upper limit in altitude than from the event in 2006, where a significant amount of water vapor reached an altitude of about 4000m.

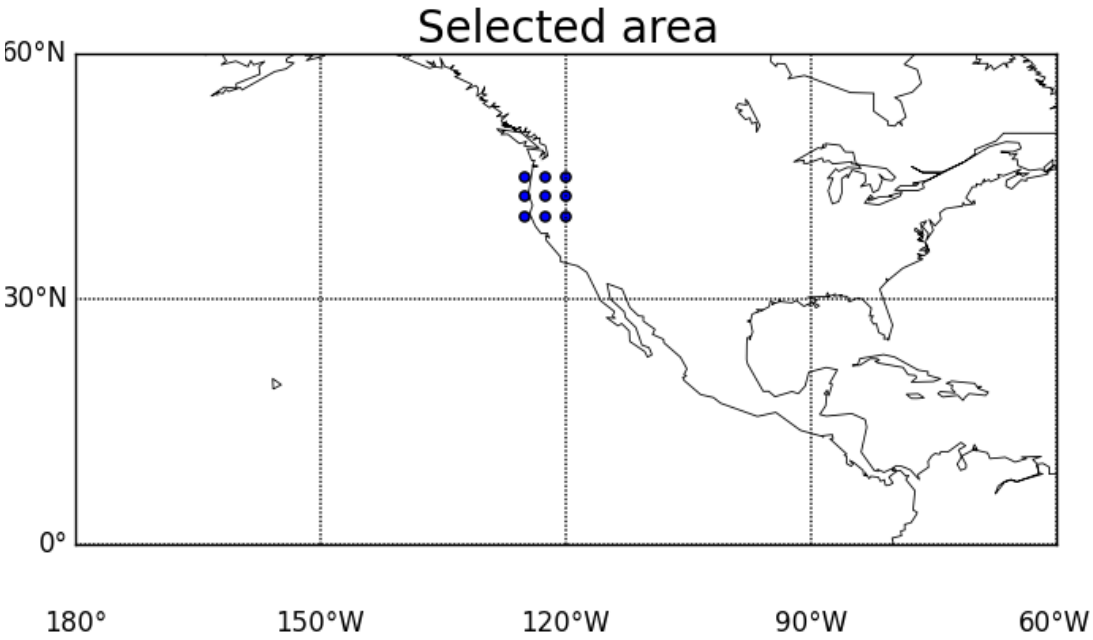

Figure 19: Map of the affected area, with the 7.5° x 7.5° grid for the arithmetic mean calculations.

During this event, the most water vapor can be found in an altitude range between 0m to 2000m and after the 13th October 2019.

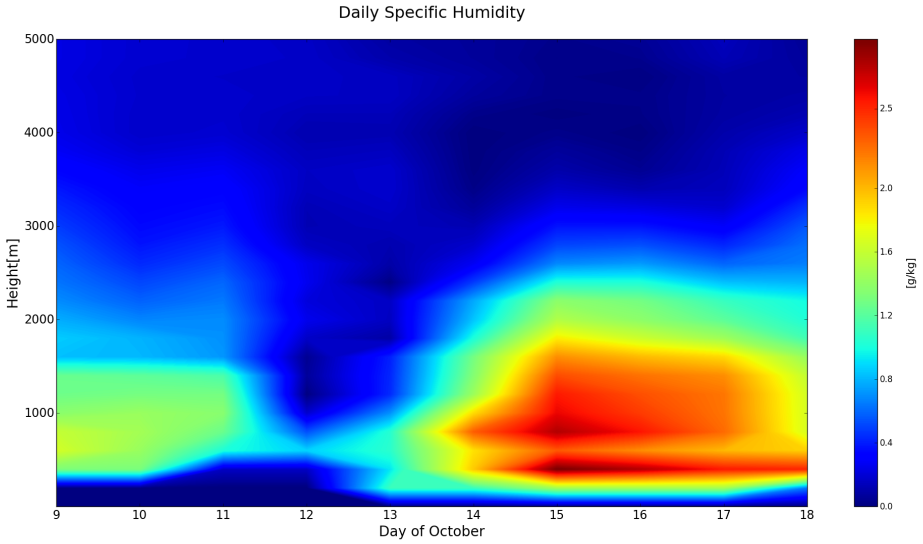

Figure 20: Height distribution of the AR event in 2009, hitting the East Coast of the United States, escpecially California.

6.5 2015 Great Britain

A further event of an AR, was the winter storm „Desmond“, which hit the British and Irish islands during the winter storm season in 2015, between the 4th and 6th December. The most affected regions of the winter storm, were the Scottish boarders as well as the northern areas of the United Kingdom, see figure 21.
A record amount of rainfall in 24 hours could be measured and therefore major floods and landslides occured.
The effects of this winter storm were catastrophic. The damage amount to 500 million pounds, and over 1000 people had to be evacuated. Because of the massive flooding and wind speeds up to 39.3 m s^{-1}, 60 000 people lost power and further on vegetation was destroyed and ground was severely eroded and washed away. [Matthews et al., 2018]
More than 100 flood warnings and more than 70 flood alerts were triggered in northern England on Saturday night, with more than 90 flood warnings and alerts in Scotland. These numbers refer to the northern region of England. In Ireland, over 2,000 people were left without power and around 700 in Wales.
The AR had it roots in the Caribbean, from where he transported moist warm air to Europe, see figure 22. Because of these enormous masses of humid air, heavy rainfalls like these can occur. [Geography, 2018]

Figure 21: The most affected regions of the AR in the UK in 2015 are marked with the red square. Further on the rivers Greta, Eden, Teviot and Kent were affected and caused for even more flooding. (Taken from Google, 2019)

On the 4th of December 341.4 mm of precipitation could be measured in Honister, Cumbria, which set a new UK record. The following figure shows our results of the calculated precipitable water, concentrating on the time period from 3th December to the 12th December. The colorbar was adapted to detect the AR, whereby over a value of 20mm the results are plotted in dark red. The AR builds up from the 3th December 2015 and reaches the islands with its devastating energy on the 4th to 5th December.

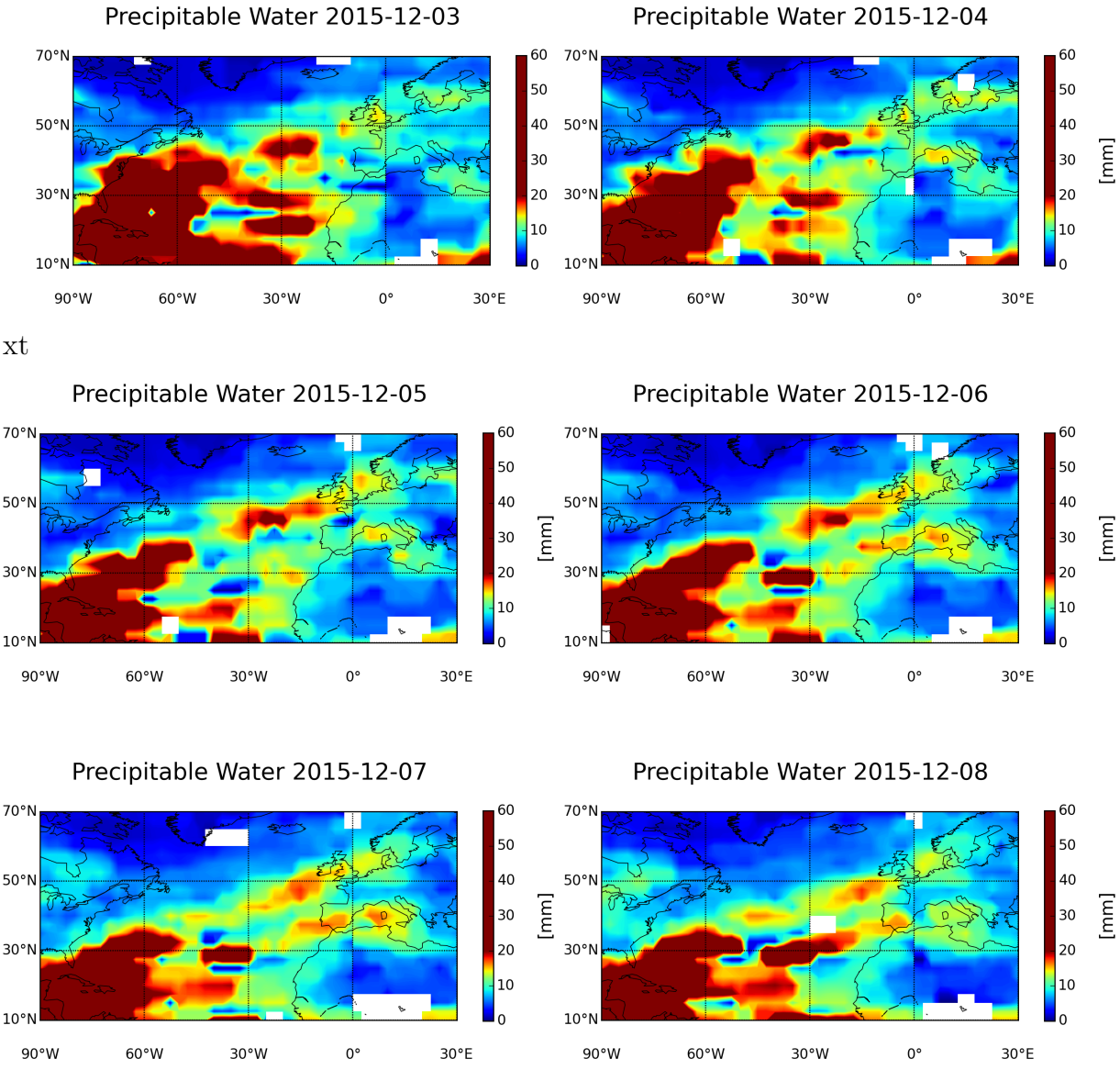

xt

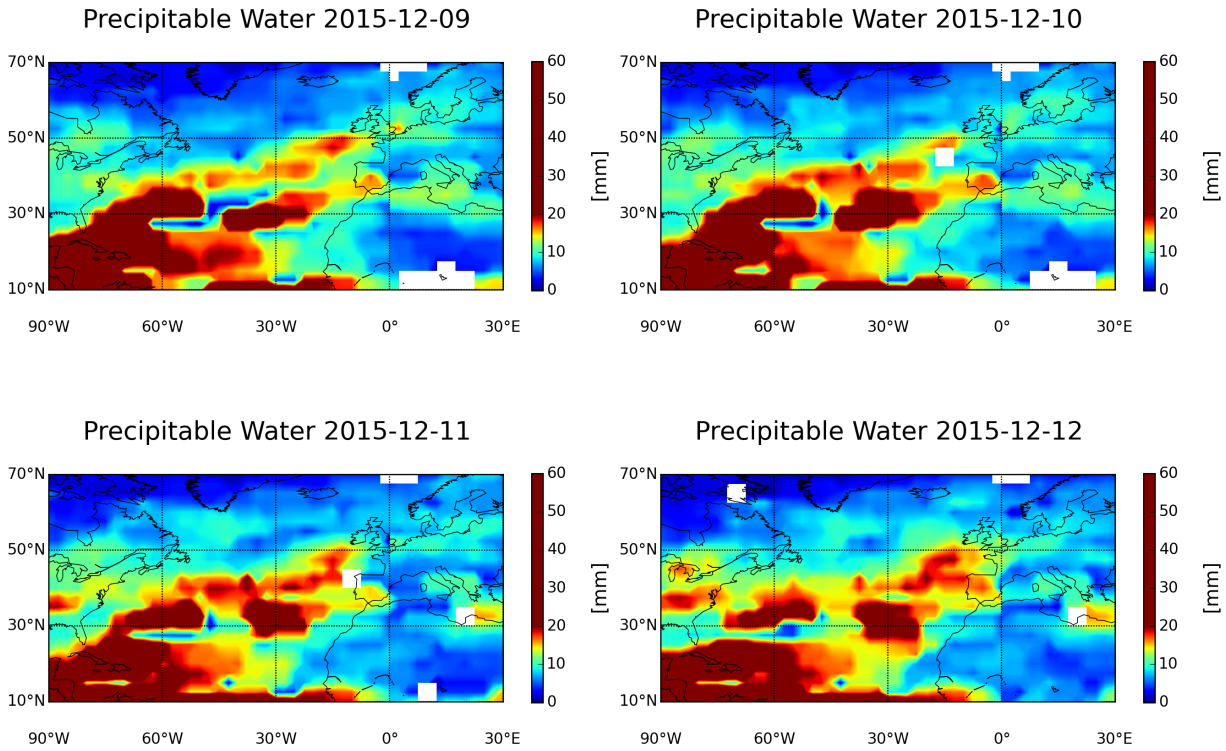

Figure 22: The AR event in 2015, where the United Kingdom as well as Ireland were hit by the Atmospheric River.

In this particular event, the influence of the climate change was investigated by Oldenborgh et al., 2015. Oldenborgh et al., 2015 used real time observations and weather analysis, historical data and climate model output to calculate the effect of the climate change. They used three different methods:

- Statistical analysis of observed trends
- coupled climate model simulations
- regional climate simulations

An area of 54°- 57°North and 6°West - 2°East is chosen, in which the likelihood, calculated on the past trends in the observations, of a 1 in a 100 year event increases by the factor of 1.3 to 2.8. The calculated factor with help of the coupled climate EC - Earth is 1.1 - 1.8 and with help of the regional climate simulations 1.05 - 1.8. So it is recognisable that the climate change has a huge influence on the likelihood of extreme weather events, such as, the AR event in 2015 in the UK. Oldenborgh et al., 2015

6.6 Height distribution - 2015 Great Britain

The AR which hit Britain in 2015 was one of the strongest and most destructive storms the island has ever hit. A 7.5° x 7.5° grid was created over this area and the water vapour content of the atmosphere was calculated for every single point and every 200 meters in height. The area has been chosen to cover the entire southern half of the island (see figure 23) and thus to draw conclusions about the impact of the atmospheric river on the affected area. Furthermore, for each height layer, the average water vapour content in g / kg was calculated and plotted over time.
The result is a plot, that allows accurate statements about the height distribution of the water vapour over the time of the extreme event. It can be seen, hat the atmospheric river is slowly building up above England and reaching full strength on 5th to 7th December 2015.
A feature of this event is that the highest concentration of the water vapour could be measured near the ground. This is in contrast to the events of 2006 and 2009, where the highest concentrations are reach in higher heights.

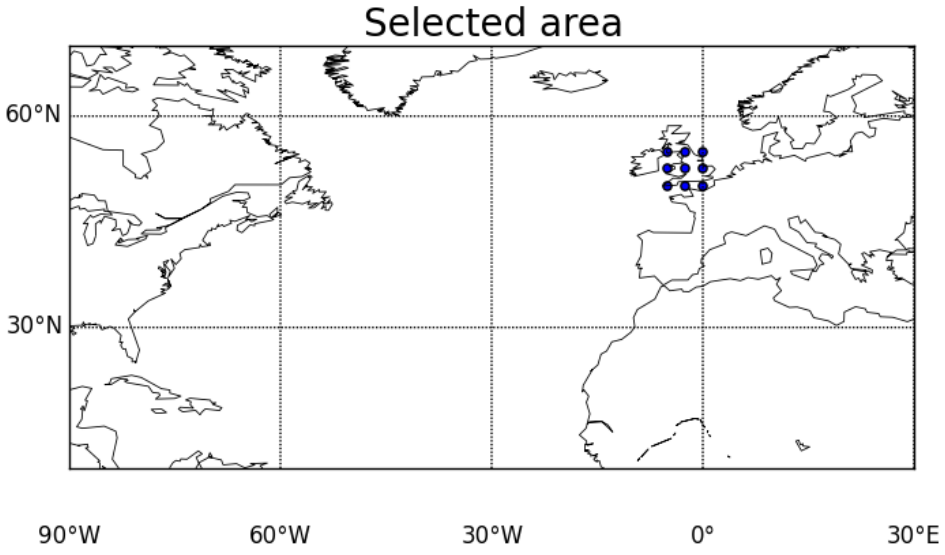

Figure 23: Map of the affected area, which was hit by the AR in December 2015 and which was used for the calculation of the height distribution of the AR.

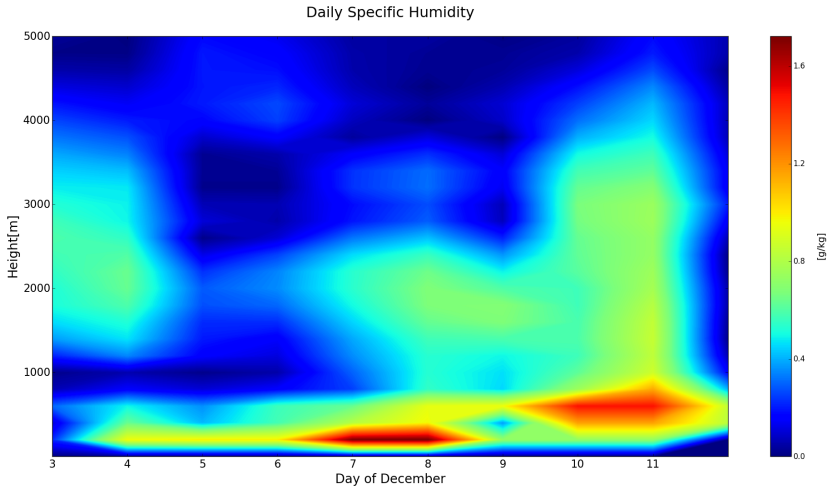

Figure 24: Water vapor distribution for the AR event in December 2015 over the chosen area.

6.7 2015 Norway

The event in December 2015 in Norway was the continuation of the AR, which had previously hit the islands of the United Kingdom and Ireland. For this reason, the source as well as the path of the AR are not described again, as this can be found in subsection 6.5. In some regions of the west coast of Norway, accumulated precipitation amounts of 300 mm could be measured. This led to numerous failures as well as disturbances in the traffic as well as to extensive flooding. The winter storm that emerged from the AR was referred to as "Synne" by the Norwegian Meteorological Institute. [Thyness et al., 2016]

To investigate the event in this thesis, a period of 10 days was chosen, in which the storm arrived on the west coast of Norway. The starting point was the 3th December 2015, because the maximum precipitation of the AR was measured between the 5th December and the 6th December 2015.
The integrated water vapor was calculated and plotted in the following figure 25. In order to assess the impact on the affected area better, the region of interest was zoomed in. Furthermore, to detect the AR, the unit of the color bar for the precipitation water was adjusted. Above 20mm of calculated precipitation, the results were shown in red on the plot.

Precipitable Water 2015-12-03

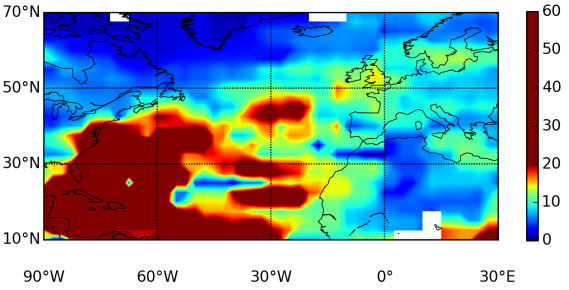

Precipitable Water 2015-12-04

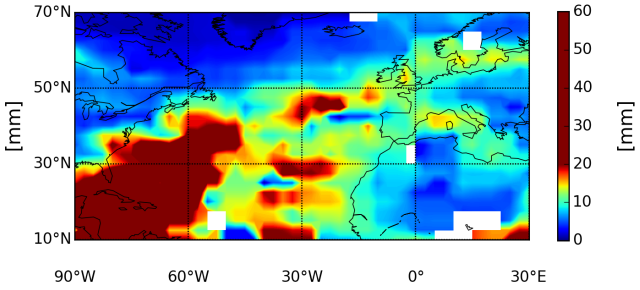

Precipitable Water 2015-12-05

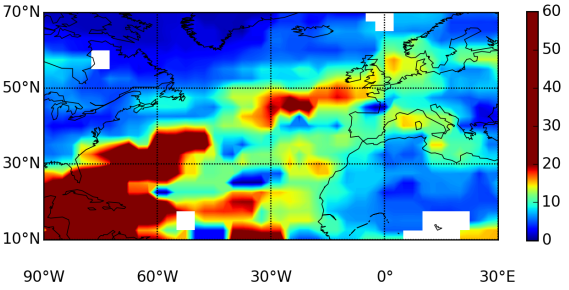

Precipitable Water 2015-12-06

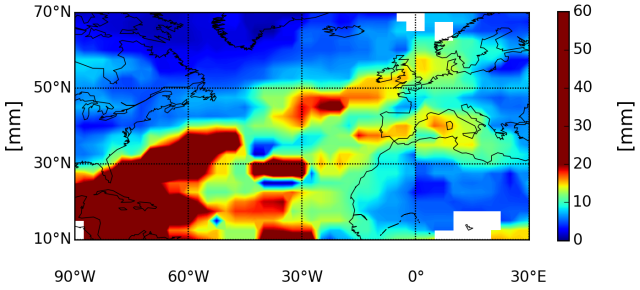

Precipitable Water 2015-12-07

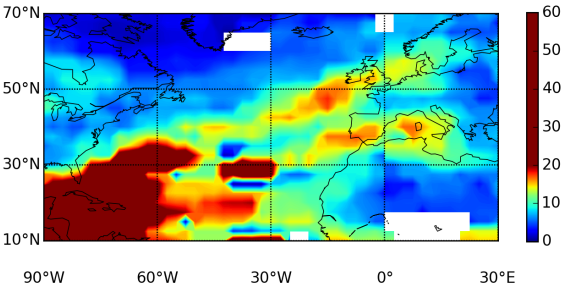

Precipitable Water 2015-12-08

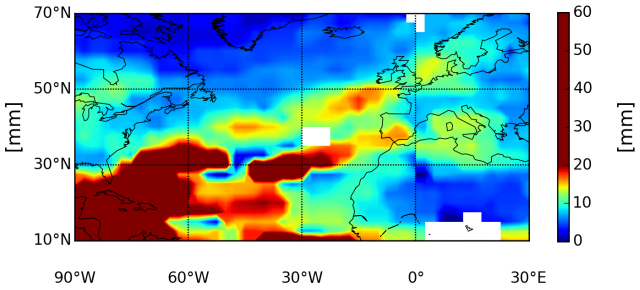

Precipitable Water 2015-12-09

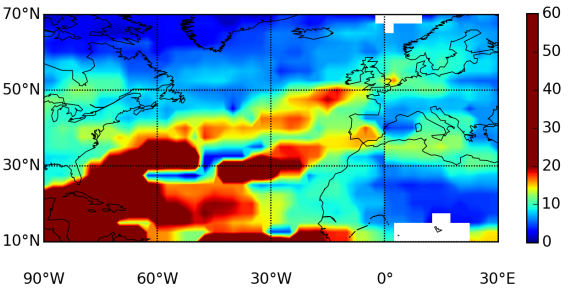

Precipitable Water 2015-12-10

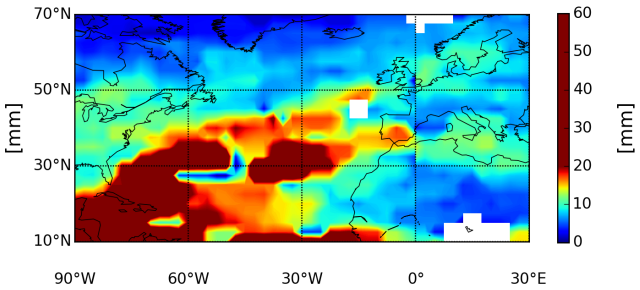

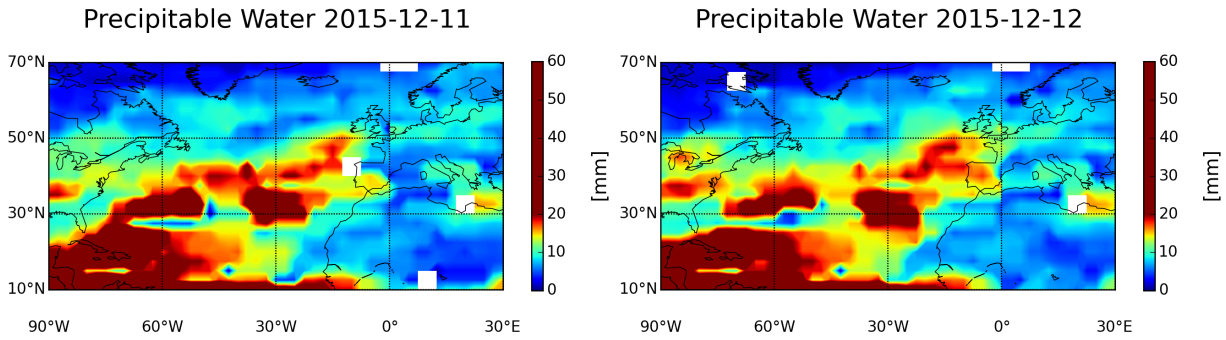

Figure 25: The AR event in 2015, where the United Kingdom as well as Ireland were hit by the Atmospheric River.

The next chapter treats the height distribution of the AR.

6.8 Height distribution - 2015 Norway

In order to examine the height distribution of the AR in Norway, a 3 x 3 grid has been set up. This corresponds to a 7.5° x 7.5° grid on the Earth , which was laid over the coastal region in the west of Norway. The grid extends from the north of Denmark to Molde, Norway. The western and eastern border of the grid are Bergen and the swedish border. It was precisely this area selected, where the AR hit land. A time series from the 3th to the 12th December 2015 was chosen, as heavy rainfall was registered in Norway on the 7th December. (see figure 26) The height distribution of water vapor is similiar to the event in Great Britain, altough the AR moved on for a few hundreds of kilometers. (see figure 27)

It can be seen that most of the water vapour can be found at an altitude up to 2000 meters. Concerning the absolute amount of water vapor, the event in UK, respectively Norway, contained much less water vapor than the events in California. The maximum amounts of water vapor in the atmosphere during the events in California 2006 and 2009, were approximately 2 g/kg and 2.8 g/kg. At the event in the UK and Norway an absolute amount of water vapor of 1.7 g/kg and 1.5 g/kg could me calculated.

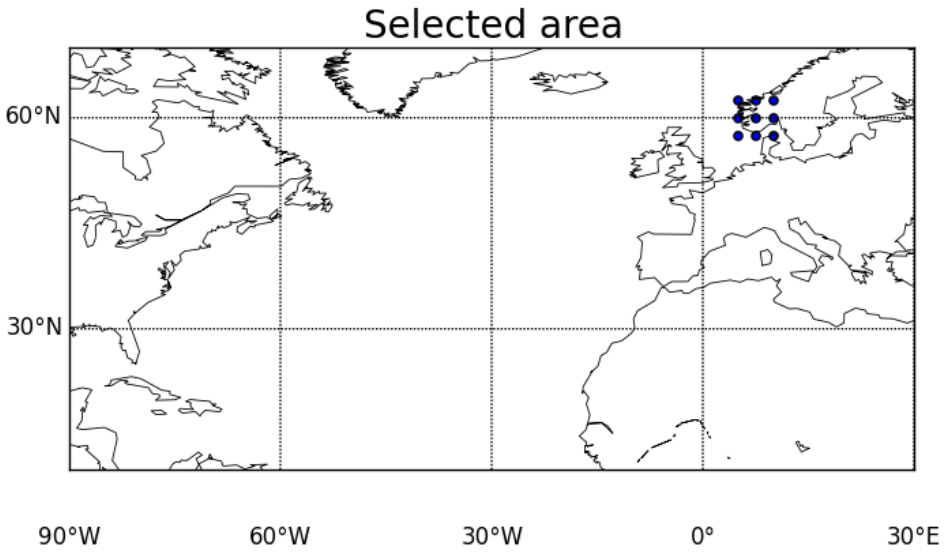

Figure 26: Map with the grid, where the arithmetic mean for each layer was calculated.

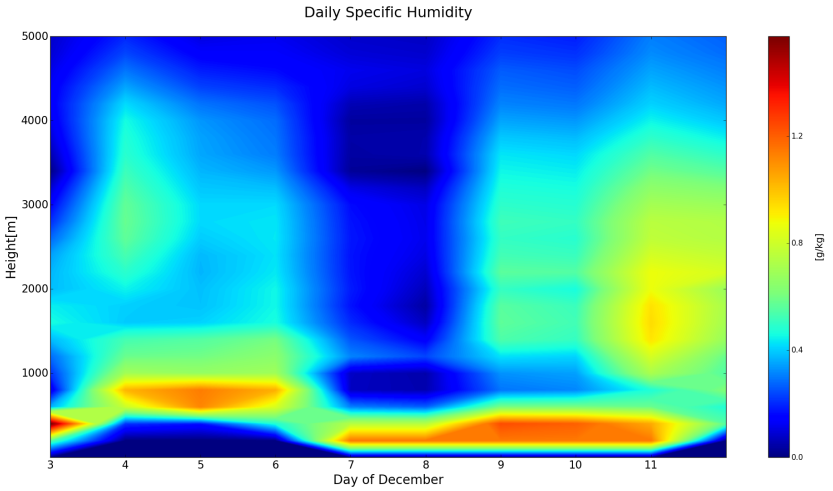

Figure 27: Height distribution of water vapor for the event in Norway 2015.

7 Summary and Conclusions

Atmospheric rivers are weather events that can cause enormous damage and it is therefore important to understand the phenomenon and to know their properties. In this thesis, these natural events were investigated and the role of AR for the people in the affected areas was examined. Furthermore, several terms for AR were explained and a short overview of the development of the definition of ARs was given.
In order, to be able to detect atmospheric rivers, data with a high vertical and horizontal resolution are necessary. So far data from radiosondes were used, but they have the disadvantage that these data are not globally available. For this reason, the Radio Occultation method is of particular interest. The main advantage of the approach to study atmospheric rivers with Radio occultation data is, that the vertical distribution of an atmospheric river can be investigated.
Further on, from the atmospheric parameters, the integrated water vapor was calculated. Radio Occultation data were used to calculate the integrated water vapor, as well as, the precipitable water. Four selected atmospheric river events were investigated in particular. Attention was paid to the following characteristics of the AR:

- The four selected atmospheric river events were divided into two events hitting the coast of Europe and two events hitting the western coast of the United States.
- Furthermore, attention was paid to the vertical distribution of the AR. The height distribution provides information about the levels at which most of the water vapor can be found.
- Finally, the temporal evolution of each event was addressed, which in turn has an influence on the serious damage in the affected areas.

Each event of the four selected is different in its own way. However, looking at the vertical distribution of the two events in Europe and the two events in the United States, similarities between the two events of each continent are detected.
The water vapor in the atmosphere reaches much higher latitudes at the events in the United states, than at the events in Europe. During the events in Europe, the most water vapor is detected below 1000 m. During the events in the United States, the most amount of water vapor reaches altitudes up to 2000 or even 3000 meters. An explanation for this could be, that the Rocky mountains form an obstacle and therefore the water vapor is forced to develop in higher altitudes.

Furthermore, the maximum amount of water vapor in the atmosphere varies from event to event. The highest concentrations of water vapor in the atmosphere was detected during the event in 2009, where an amount of 3 g/kg on the 15^{th} of October was detected.

Acronyms

AR Atmospheric River

CHAMP Challenging Minisatellite Payload

COSMIC Constellation Observing System for Meteorology, Ionosphere, and Climate

DOD United States Department of Defense

ECMWF European Centre for Medium-Range Weather Forecasts

EU European Union

ESA European Space Agency

GLONASS Global'naya Navigatsionnaya Sputnikovaya Sistema / Global Navigation Satellite System

GNSS Global Navigation Satellite System

GPS Global Positioning System

GPS/MET Global Positioning System?Meteorology

IWV Integrated Water Vapor

LEO Low Earth Orbit

MEO Mid Earth Orbit

Nasa National Aeronautics and Space Administration

NOAA National Oceanic and Atmospheric Administration

PW Precipitable Water

RO Radio Occultation

US United States

USA United States of America

VKO Russian Voyska Vozdushno-Kosmicheskoy Oborony / Aerospace Defense Forces

WEGC Wegener Center for Climate and Global Change [University of Graz]

WV Water Vapor

List of Figures

List of Tables

References

[Anthes et al., 2008] Anthes, R. A., Bernhardt, P. A., Chen, Y., Cucurull, L., Dymond, K. F., Ector, D., Healy, S. B., Ho, S. P., Hunt, D. C., Kuo, Y.-H., Liu, H., Manning, K., McCormick, Meehan, T. K., Randel, W. J., Rocken, C., Sokolovskiy, W. S. S. S. V., Syndergaard, S., Thompson, D. C., Trenberth, K. E., Wee, T. K., Yen, N. L., and Zeng, Z. (2008). The cosmic/formosat-3 mission: Early results. *Bulletin of the American Meteorological Society, Vol. 89*.

[Anthes et al., 2000] Anthes, R. A., Rocken, C., and Kuo, Y. H. (2000). Application of cosmic to meteorology and climate. *Terrestrial, Atmospheric and Oceanic Sciences, Vol.11*.

[Auyeung, 2019] Auyeung, C. (2019). Phase diagram for water - ck-12 foundation. https://www.ck12.org/chemistry/phase-diagram-for-water/lesson/Phase-Diagram-for-Water-CHEM/. Accessed: 2019-05-01.

[Behrangi et al., 2016] Behrangi, A., Guan, B., Neiman, P. J., Schreier, M., and Lambrigtsen, B. (2016). On the quantification of atmospheric rivers precipitation from space: Composite assessments and case studies over the eastern north pacific ocean and the western united states. *Journal of Hydrometeorology*, 4:369 – 382.

[Brunner et al., 2016] Brunner, L., Steiner, A. K., Scherllin-Pirscher, B., and Jury, M. W. (2016). Exploring atmospheric blocking with gps radio occultation observations. *Atmospheric Chemistry and Physics*, 4593-4604.

[Chesters, 2014] Chesters, D. (2014). Satellite animation shows return of the pineapple express. https://www.nasa.gov/content/goddard/satellite-animation-shows-return-of-the-pineapple-express/. Accessed: 2019-02-15.

[Danzer et al., 2013] Danzer, J., Scherllin-Pirscher, B., and Foelsche, U. (2013). Systematic residual ionospheric errors in radio occultation data and a potential way to minimize them. *Atmos. Meas. Tech.*, 6.

[Dettinger, 2004] Dettinger, M. (2004). Fifty-two years of pineapple express storms across the west coast of north america.

[Dettinger, 2011] Dettinger, M. (2011). Climate change, atmospheric rivers and floods in california - a multimodel analysis of storm frequency and magnitude changes. *Journal of the american water ressources association*.

[Dettinger and Ingram, 2013] Dettinger, M. and Ingram, B. L. (2013). The coming megafloods. *Scientific American*.

[Dvorsky, 2017] Dvorsky, G. (2017). Dramatic satellite photo shows an'atmospheric river drenching california. https://gizmodo.com/dramatic-satellite-photo-shows-an-atmospheric-river-dre-1792631906. Accessed: 2019-02-15.

[Fears, 2015] Fears, D. (2015). Sky me a river: Scientists say flood threat linked to atmospheric rivers. https://www.washingtonpost.com/news/energy-environment/wp/2015/01/26/a-river-runs-above-it-noaa-tries-to-predict-floods-by-studying-rivers-in-the-sky/?noredirect=on&utm_term=.646c7cb7ad38. Accessed: 2019-02-25.

[Fischetti, 2018] Fischetti, M. (2018). Atmospheric river could trigger big california mudslides. https://www.scientificamerican.com/article/atmospheric-river-could-trigger-big-california-mudslides/. Accessed: 2019-02-15.

[Fjeldbo et al., 1971] Fjeldbo, G., Kliore, A. J., and Eshleman, V. R. (1971). The neutral atmosphere of venus as studied with the mariner v radio occultation experiments. *The Astronomical Journal*.

[Foelsche, 1999] Foelsche, U. (1999). *Tropospheric water vapor imaging by combination of ground-based and spaceborne GNSS sounding data*. PhD thesis, University of Graz.

[Foelsche, 2017] Foelsche, U. (2017). Lecture university of graz: Meteorology. *University of Graz*.

[Foelsche et al., 2011] Foelsche, U., Scherllin-Pirscher, B., Ladstädter, F., Steiner, A. K., and Kirchengast, G. (2011). Refractivity and temperature climate records from multiple radio occultation satellites consistent within 0.05 %. *Atmospheric Measurement Techniques 4*.

[Gaffen et al., 1992] Gaffen, D. J., Elliot, W., and Robock, A. (1992). Relationships between tropospheric water vapor and surface temperature as observed by radiosondes. *Geophysical Research Letters*.

[Galewsky and Sobel, 2005] Galewsky, J. and Sobel, A. (2005). Moist dynamics and orographic precipitation in northern and central california during the new year's flood of 1997. *MONTHLY WEATHER REVIEW*, 133:1594 – 1612.

[Geography, 2018] Geography (2018). A level geography. http://www.alevelgeography.com/storm-desmond-case-study/. Accessed: 2019-03-01.

[Google, 2019] Google (2019). Google maps. https://www.google.com/maps. Accessed: 2019-05-01.

[Gorbunov et al., 2004] Gorbunov, M. E., Benzon, H. H., Jensen, A. S., Lohmann, M. S.,

and Nielsen, A. S. (2004). Comparative analysis of radio occultation processing approaches based on fourier integral operators. *RADIO SCIENCE*, 39.

[Gorbunov et al., 2000] Gorbunov, M. E., Gurvich, A. S., and Kornblueh, L. (2000). Comparative analysis of radioholographic methods of processing radio occultation data. *Journal of Geophysical Research*.

[Greenmind, 2016] Greenmind (2016). Precipitation. https://commons.wikimedia.org/wiki/File:Precipitation_longterm_mean.gif. Accessed: 2019-02-15.

[Hajj et al., 2002] Hajj, G. A., Kursinski, E. R., Romans, L. J., Bertiger, W. I., and Leroy, S. S. (2002). A technical description of atmospheric sounding by gps occultation. *Journal of Atmospheric and Solar-Terrestrial Physics*, 64-4:451–469.

[Hayes, 2012] Hayes, D. (2012). The neutral atmosphere of venus as studied with the mariner v radio occultation experiments. Website. "http://www.oosa.unvienna.org/pdf/icg/2012/icg-7/4.pdf".

[Khélifa et al., 2007] Khélifa, N., Lecollinet, M., and Himbert, M. (2007). Molar mass of dry air in mass metrology. *Measurement*, 40:779–784.

[Kramer, 2002] Kramer, H. J. (2002). *Survey of Missions and Sensors*. Springer-Verlag Berlin Heidelberg.

[Kuo et al., 2004] Kuo, Y.-H., Wee, T.-K., Sokolovskiy, S., Rocken, C., Schreiner, W., D. Hunt, D., and Anthes, R. A. (2004). Inversion and error estimation of gps radio occultation data. *Journal of the Meteorological Society of Japan, Vol. 82*.

[Kursinski et al., 1997] Kursinski, E. R., Hajj, G. A., Schofield, J. T., Linfield, R. P., and Hardy, K. R. (1997). Observing earth's atmosphere with radio occultation measurements using the global positioning system. *Journal of Geophysical Research*.

[Lavers et al., 2011a] Lavers, D. A., Allan, R. P., Wood, E. F., , Villarini, G., Brayshaw, D. J., and Wade, A. J. (2011a). Winter floods in britain are connected to atmospheric rivers. *Geophysical Research Letter*, 38.

[Lavers et al., 2011b] Lavers, D. A., Allan, R. P., Wood, E. F., Villarini, G., Brayshaw, D. J., and Wade, A. J. (2011b). Winter floods in britain are connected to atmospheric rivers. *Geophysical Research Letters Vol 38.*

[Leung and Qian, 2009] Leung, L. R. and Qian, Y. (2009). Atmospheric rivers induced heavy precipitation and flooding in the western u.s. simulated by the wrf regional climate model. *Geophys. Res. Lett.*, 36.

[Liljequist and Cehak, 1984] Liljequist, G. H. and Cehak, K. (1984). *Allgemeine Meteorologie*. Vieweg & Sohn.

[Ma, 1998] Ma, Q. (1998). Greenhouse gases: Refining the role of carbon dioxide. https://www.giss.nasa.gov/research/briefs/ma_01/. Accessed: 2019-02-15.

[Markings, 2017] Markings, S. (2017). Percentage of water vapor in the atmosphere. Website. "https://sciencing.com/percentage-water-vapor-atmosphere-19385.html".

[Matthews et al., 2018] Matthews, T., Murphy, C., McCarthy, G., Broderick, C., and Wilby, R. L. (2018). Super storm desmond: A process-based assessment. *Environmental Research Letters*, 13.

[Melbourne et al., 1994] Melbourne, W. G., Davis, E. S., Duncan, C. B., Hajj, G. A., Hardy, K. R., Kursinski, E. R., Meehan, T. K., Young, L. E., and Yunck, T. P. (1994). The application of spaceborne gps to atmospheric limb sounding and global change monitoring. *JPL Publication*, 94-18, 147.

[Mohr et al., 2008] Mohr, P. J., Taylor, B. N., and Newell, D. B. (2008). Codata recommended values of the fundamental physical constants: 2006. *REVIEWS OF MODERN PHYSICS*, 80:663–730.

[Neiman et al., 2013a] Neiman, P. J., Hughes, M., Moore, B. J., Ralph, F. M., and and, E. M. S. (2013a). Sierra barrier jets, atmospheric rivers, and precipitation characteristics in northern california: A composite perspective based on a network of wind profilers. *American Meteorological Society*, pages 4211–4233.

[Neiman et al., 2008a] Neiman, P. J., Ralph, F., Wick, G., Kuo, Y.-H., Wee, T.-K., Z. Ma, G. T., and Dettinger, M. (2008a). Diagnosis of an intense atmospheric river impacting the pacific northwest: Storm summary and offshore vertical structure observed with cosmic satellite retrievals. *MONTHLY WEATHER REVIEW*, 136:4398–4420.

[Neiman et al., 2013b] Neiman, P. J., Ralph, F. M., Moore, B. J., Hughes, M., Mahoney, K. M., Cordeira, J. M., and Dettinger, M. D. (2013b). The landfall and inland penetration of a flood-producing atmospheric river in arizona. part i: Observed synoptic-scale, orographic, and hydrometeorological characteristics. *Journal of Hydrometeorology Vol 14.*

[Neiman et al., 2008b] Neiman, P. J., Ralph, F. M., Wick, G. A., Lundquist, J. D., and Dettinger, M. (2008b). Meteorological characteristics and overland precipitation impacts of atmospheric rivers affecting the west coast of north america based on eight years of ssm/i satellite observations. *Journal of Hydrometeorology Vol. 9.*

[.Neiman et al., 2011] .Neiman, P. J., Schick, L. J., Ralph, F. M., Hughes, M., and Wick, G. A. (2011). Flooding in western washington: The connection to atmospheric

rivers. *JOURNAL OF HYDROMETEOROLOGY*, 12:1337–1358.

[Neiman et al., 2011] Neiman, P. J., Schick, L. J., Ralph, F. M., Hughes, M., and Wick, G. A. (2011). Flooding in western washington: The connection to atmospheric rivers. *Journal of Hydrometeorology Vol 12.*

[NOAA, 2015a] NOAA (2015a). The science behind atmospheric rivers. Website. "http://www.noaa.gov/sites/default/files/thumbnails/image/atmosphericrivers_final.jpg".

[NOAA, 2015b] NOAA (2015b). The science behind atmospheric rivers. Website. "http://www.noaa.gov/sites/default/files/thumbnails/image/atmosphericrivers_final.jpg".

[Oldenborgh et al., 2015] Oldenborgh, G. J. V., Otto, F. E. L., Haustein, K., and Cullen, H. (2015). Climate change increases the probability of heavy rains like those of storm desmond in the uk ? an event attribution study in near-real time. *Hydrology and Earth System Sciences Discussions*, 12.

[Peixoto and Oort, 1992] Peixoto, J. P. and Oort, A. H. (1992). *Physics of climate*. American Inst. of Physics.

[Ralph and Dettinger, 2010] Ralph, F. M. and Dettinger, M. (2010). Historical and national perspectives on extreme west coast precipitation associated with atmospheric rivers during december 2010. *Bulletin of the American Meteorological Society Vol 93.*

[Ralph et al., 2011] Ralph, F. M., Neiman, P. J., Kiladis, G. N., Weickman, K., and Reynolds, D. W. (2011). A multi-scale observational case study of a pacific atmospheric river exhibiting tropical-extratropical connections and a mesoscale frontal wave. *MONTHLY WEATHER REVIEW*, 139:1169–1189.

[Ralph et al., 1961] Ralph, F. M., Neiman, P. J., Wick, G. A., Gutman, S. I., Dettinger, M. D., Cayan, D. R., and White, A. B. (1961). Flooding on california's russian river: Role of atmospheric rivers. *Geophysical Research Letters, Vol. 33.*

[Ramos et al., 2016] Ramos, A. M., Tomé, R., Trigo, R. M., Liberato, M. L. R., and Pinto, J. G. (2016). Projected changes in atmospheric rivers affecting europe in cmip5 models. *Geophysical Research Letter*, 43.

[Rutz and Steenburgh, 2012] Rutz, J. J. and Steenburgh, W. J. (2012). Quantifying the role of atmospheric rivers in the interior western united state. *Atmospheric Scientific Letters Vol 13.*

[Scherllin-Pirscher et al., 2011] Scherllin-Pirscher, B., Kirchengast, G., Steiner, A. K., Kuo, Y. H., and Foelsche, U. (2011). Quantifying uncertainty in climatological fields from gps radio occultation: an empirical-analytical error model. *Atmospheric Measurement Techniques Discussions*, 4:2749–2788.

[Schwärz et al., 2013] Schwärz, M., Scherllin-Pirscher, B., Kirchengast, G., Schwarz, J., Ladstädter, F., Fritzer, J., and Ramsauer, J. (2013). Multi-mission validation by satellite radio occultation. *Wegener Center?Uni Graz Final Report for ESA?ESRIN No. 01?2013*, 136:111–128.

[Seguin, 2012] Seguin, W. (2012). American meteorological society - barrier jet. http://glossary.ametsoc.org/wiki/Barrier_jet. Accessed: 2019-03-04.

[Smith et al., 2010] Smith, B. L., Yuter, S., Neiman, P., and Kingsmill, D. (2010). Water vapor fluxes and orographic precipitation over northern california associated with a landfalling atmospheric river. *MONTHLY WEATHER REVIEW*, 138:74–100.

[Smith and Weintraub, 1953] Smith, E. and Weintraub, S. (1953). The constants in the equation for atmospheric refractive index at radio frequencies. *Proceedings of the IRE 41*, pages 1035–1037.

[Staff, 2007] Staff, N. (2007). Greenhouse gases and water vapor: When 'positive feedback' is a bad thing. https://www.science20.com/news_account/greenhouse_gases_and_water_vapor_when_positive_feedback_is_a_bad_thing. Accessed: 2019-03-04.

[Steiner et al., 2011] Steiner, A., Lackner, B. C., Foelsche, U., Ladstädter, F., Scherllin-Pirscher, B., and Kirchengast, G. (2011). Gps radio occultation for climate monitoring and change detection. *Radio American*.

[Steiner, 1998] Steiner, A. K. (1998). High resolution sounding of key climate variables using the radio occultation technique. *PhD thesis. University of Graz, Austria: Institute for Geophysics, Astrophysics, and Meteorology*.

[Stocker et al., 2013] Stocker, T. F., D. Qin, G.-K. P., Tignor, M., Allen, S. K., Boschung, J., Nauels, A., Xia, Y., Bex, V., and Midgley, P. M. (2013). Climate change 2013: The physical science basis. contribution of working group i to the fifth assessment report of the intergovernmental panel on climate change. *Cambridge University Press*.

[Stohl et al., 2008] Stohl, A. C., Forster, C., and Sodemann, H. (2008). Remote sources of water vapor forming precipitation on the norwegian west coast at 60° n - a tale of hurricanes and an atmospheric river. *Journal of Geophysical Research*, 113.

[Syndergaard, 2000] Syndergaard, S. (2000). On the ionosphere calibration in gps radio occultation measurements. *Radio Science, Vol. 35*.

[Thyness et al., 2016] Thyness, V., Homleid, M., Haugen, G. M., and Seierstad, I. (2016). Application and verification of ecmwf products 2016. *Norwegian Meteorological Institute*.

[UCAR, 2017] UCAR, C. P. (2017). Eighth FORMOSAT-3/COSMIC Data Users' Workshop. https://www.cosmic.ucar.edu/workshop_2014/. Accessed: 2019-02-13.

[Union, 2013] Union, A. G. (2013). Atmospheric rivers linked to severe precipitation in western europe. Website. "https://phys.org/news/2013-07-atmospheric-rivers-linked-severe-precipitation.html".

[Ware et al., 1996] Ware, R., Exner, M., Feng, D., Gorbunov, M., Hardy, K., Herman, B., Kuo, Y.-H., Meehan, T., Melbourne, W., Rocken, C., Schreiner, W., Sokolovskiy, S., Solheim, F., Zou, X., Anthes, R., Businger, S., and Trenberth, K. (1996). Gps sounding of the atmosphere from low earth orbit: Preliminary results. *Bull. Amer. Meteor. Soc.*

[Weaver, 1962] Weaver, R. L. (1962). Meteorology of hydrologically critical storms in california. *Hydrol. Rep. 37, 207 pp.*

[Zhu and Newell, 1998] Zhu, Y. and Newell, R. E. (1998). A proposed algorithm for moisture fluxes from atmospheric rivers. *Monthly weather review*.

[Zhu et al., 1992] Zhu, Y., Newell, R. E., Scott, C., and Newell, N. E. (1992). Tropospheric rivers? - a pilot study. *Geophysical Research Letters*.